LASER NANO-STRUCTURING DEEP INSIDE SILICON USING BESSEL BEAMS

A THESIS SUBMITTED TO

THE GRADUATE SCHOOL OF ENGINEERING AND SCIENCE

OF BILKENT UNIVERSITY

IN PARTIAL FULFILLMENT OF THE REQUIREMENTS FOR

THE DEGREE OF

MASTER OF SCIENCE

IN

MATERIALS SCIENCE AND NANOTECHNOLOGY

By

Aqiq Ishraq

January 2021

Laser nano-structuring deep inside silicon using Bessel beams

By Aqiq Ishraq

January 2021

We certify that we have read this thesis and that in our opinion it is fully adequate, in scope and in quality, as a thesis for the degree of Master of Science.

Onur Tokel(Advisor)

Hilmi Volkan Demir

Emre Yüce

Approved for the Graduate School of Engineering and Science:

Ezhan Karaşan
Director of the Graduate School

ABSTRACT

LASER NANO-STRUCTURING DEEP INSIDE SILICON USING BESSEL BEAMS

Aqiq Ishraq
M.S. in Materials Science and Nanotechnology
Advisor: Onur Tokel
January 2021

Current nano-fabrication methods for silicon (Si), while excellent, are limited to its surface. Novel laser-lithography methods are emerging to introduce subsurface (in-chip) functionality to Si, however, the state-of-the-art is at the microfabrication level, with resolution limited to > 1 µm. Multiple challenges exist for breaking this fabrication barrier, such as the diffraction-limit and complex limiting nonlinear effects inside silicon. This thesis demonstrates the first nanofabrication capability deep inside silicon, achieved without altering the wafer above or below fabricated structures, with confinement in one- and two-dimensions at the nanoscale. We achieve this by exploiting nonlinear energy localization due to structured laser beams and also a new seeding-type effect. The approach is based on pre-formed laser-written in-chip structures enabling the controlled formation of even smaller features. We also demonstrate laser polarization as a new parameter for in-chip fabrication control. Further, by exploiting a combination of parameters, including pulse energy, Bessel beam phase pattern, polarization and the laser focusing conditions, we demonstrate the first in-chip structures that are beyond the diffraction limit in terms of feature size, with resolution down to 120 nm ± 25 nm, thus, improving the state-of-the-art by about an order of magnitude. In order to demonstrate a proof-of-concept optical element, we fabricated the first in-chip nano-gratings, shown to be operating with an efficiency approaching 90%. This new nanofabrication capability, demonstrated for the important technological material silicon, may have significant implications for nano-photonics, micro/nano-fluidics, photonic-electronic integration, and micro/nano-electromechanical systems (MEMS/NEMS)-type systems.

Keywords: Laser-writing, in-chip photonics, silicon photonics, nanofabrication.

ÖZET

BESSEL IŞINI KULLANILARAK SILISYUM DERINLIKLERINDE LAZER NANO-YAPILANDIRMASI

Aqiq Ishraq
Malzeme Bilimleri ve Nanoteknoloji, Yüksek Lisans
Tez Danışmanı: Onur Tokel
January 2021

Silisyum (Si) için mevcut üretim yöntemleri, son derece gelişmiş olmalarına rağmen, sadece yonganın yüzeyi üzerinde kullanılmaktadırlar. Yüzey altı (yonga-içi) işlevsellik kazanmak için özgün üç-boyutlu lazer-yazma yöntemleri geliştirilmekte, fakat bu yöntemler mikro-üretim seviyesinde kalmakta ve 1-µm çözünürlük ile kısıtlı olmaktadırlar. Bu çözünürlük sınırını aşmak için, kırınım-sınırı ve yonga içerisinde karmaşık doğrusal-olmayan etkiler gibi çeşitli problemler bulunmaktadır. Bu tez, Si yonganın derinliklerinde ilk nano-üretim kabiliyetini göstermektedir. Elde edilen lazer-ile-yazılmış yapılar, yonganın yüzeylerine müdahale edilmeden üretilmekte, bir ve iki boyutta (1B ve 2B) kısıtlanmış yapıları nano-rejimde üretmeye olanak sağlamaktadır. Bu özgün üretim kabiliyetine, biçimlendirilmiş lazer demetleri kullanarak ve yeni gözlemlediğimiz bir tür tohumlama etkisi ile ulaştık. Bu yaklaşım, önceden oluşturulan çeşitli yonga-içi yapıların, bir çeşit tohumlama etkisi ile, çok daha küçük boyutlarda yapı üretilmesine izin vermesi ile mümkün olmuştur. Aynı zamanda, lazer polarizasyonunu yonga-içi yazım kontrolü için yeni bir parametre olarak gösterdik. Ayrıca, lazer atım süresi, demet faz deseni, polarizasyon ve lazer odaklanma şartları gibi parametrelerden faydalanarak, yonga-içinde kırınım-sınırının altında, çözünürlüğü 120 nm $\pm$ 25 nm olan yapıların üretimini gösterdik. Bu şekilde son teknoloji yonga-içi üretim çözünürlüğünü yaklaşık on kat ileriye taşıdık. Bu yaklaşım ile kavramsal seviyede bir optik eleman göstermek amacı ile yonga-içi bir demek ızgarası ürettik ve %90'a varan verimle çalıştığını gösterdik. Teknolojik olarak önemli Si için bu yeni üretim kabiliyetinin, nano-fotonik, mikro/nano-akışkanlar, fotonik-elektronik entegrasyonu ve mikro / nano-elektromekanik (MEMS/NEMS) uygulamalar için de önemli bir potansiyele sahip olduğu değerlendirilebilir.

Anahtar sözcükler: Lazer-yazım, yonga içi fotonik, silisyum fotonik, nano-üretim.

Acknowledgement

I would like to first thank my thesis advisor Dr. Onur Tokel for his amazing support throughout my research. Dr. Tokel was always available for feedback and guidance whenever I faced any challenges in my work. It was a privilege working with him, and his mentorship helped me immensely in my professional development as a researcher. I am very grateful for the opportunity to have him as my advisor.

I would also like to extend my gratitude to my colleague Dr. Rana Asgari Sabet for her continuous support. I would like to acknowledge her contribution to this work, particularly for her efforts in beam simulation and analysis. I would like to thank my colleagues Dr. Ahmet Turnalı, Muhammad Ahsan Tauseef, and Alperen Saltık for their support. I enjoyed our many scientific and non-scientific discussions that made the entire journey fun. I would also like to thank Dr. F. Ömer Ilday and my colleagues from his laboratory for their support at various stages.

I would also like to thank my respectable jury members Dr. H. Volkan Demir and Dr. Emre Yüce for taking the time to be a part of my committee and reviewing this thesis.

I am indebted to my loving parents and my sister Marzana Ishraq for their unconditional love and support.

Last but not least, I must express my profound gratitude to my beloved wife Nazifa Tasnim Arony. Without her tireless love and support, this journey would not have been possible. I will treasure all the intellectual discussions we had throughout this work and I appreciate all her sacrifices that allowed me to successfully complete this study.

Contents

List of Figures

List of Tables

Chapter 1

Introduction

Silicon is arguably the most important material for modern technology, with extremely wide applications in microelectronics and optoelectronics. Modern micro- and nanofabrication techniques opened doors to diverse applications ranging from sensors, medical diagnostics, and most recently silicon-photonics. Silicon photonics is potentially a disruptive technology with the key advantage of unifying silicon-based photonic devices with conventional electronics. A key advantage is the high speed and lossless propagation of light, motivating the rapid growth towards stand-alone and integrated photonic components and circuits on silicon. Silicon stands apart from common dielectrics and crystals such as silica and lithium niobate, as it is Complementary-Metal-Oxide-Semiconductor (CMOS) compatible, which is the fundamental work-horse of microelectronics industry. The potential of integrating optics on this substrate was recognized early, but with significant obstacles to be overcome. In this thesis, we will provide a complementary approach to such conventional fabrication and integration approaches, providing a significant potential for further exploitation of this technologically important material. Silicon is a semiconductor which offers tunable properties through manipulation of its free charge carriers by doping. Modern micro- and nano-fabrication techniques exploited this property, to tailor the refractive index and band gap of silicon, in order to demonstrate novel optical devices such as the first silicon waveguides in 1989 [1]. Emergence of modern lithography techniques applied to the Silicon-on-Insulators (SOI) platform subsequently resulted in novel micro- and nano-devices for the advanced control and behaviour of light in silicon [2,3]. A key limitation remains, in that, modern lithography techniques are applied virtually exclusively on the wafer surface. This prevents the use of the large volume of the wafer, and limits the creation of optical components and circuits to the top thin layer of silicon. While extremely successful, surface fabrication is expensive, time intensive and requires an ultra-clean environment. Recently, laser-based fabrication techniques are emerging to overcome these issues, while achieving 3D control in the bulk of silicon at the microscale. These direct fabrication methods are enabling new possibilities inside the bulk of the wafer, such as buried waveguides, optical gratings, holography, and subsurface microfluidic channels for integrated cooling [4–8]. Next, we will review these emerging approaches, their potential, limitations, and then introduce our novel laser-writing approach to push the boundaries.

1.1 3D direct laser writing deep inside silicon

Direct laser writing (DLW) techniques for controlling optical properties in the bulk of transparent materials have wide applications. Early examples go back to the demonstration of ultrafast-laser-written waveguides inside glass, demonstrated by Davis et al. in 1996 [9]. Subsequently, high aspect ratio microfluidic channels were fabricated in fused silica using a combination of ultrafast laser writing and chemical etching, paving the way for affordable microsystem production in transparent media [10]. Later advances have shown a large class of microsystems and optical elements fabricated inside transparent materials, including glasses, various crystals and polymers [11, 12]. Thus, it was natural to expect similar successes to be replicated in silicon; the motivations are plenty and very strong. Silicon is a CMOS compatible semiconductor, meaning that successful modification inside this material, coupled with advanced optical and electrical control, has the potential to revolutionize integrated optoelectronics technologies. Another distinct advantage over dielectrics is that, silicon is transparent at the near and mid-infrared wavelength range. Thus, optical elements can operate in the important telecommunication bands.

Early demonstrations of laser-writing on silicon focused on laser-lithography of the surface, leading to super-wicking [13] and black silicon, for applications such as in photovoltaics [14]. However, until recently, attempts to create laser-induced modifications and the fabrication of functional optical elements inside the bulk of silicon, analogous to those of in glass, had been unsuccessful. Recent studies, as described in the next section, have dramatically improved our understanding of the physical processes that take effect inside the bulk of silicon, controlled modification of the material, and the subsequent use of laser-written areas as building blocks for more complex elements with advanced functionalities.

1.1.1 Light-matter interaction - an overview

The general premise of direct-laser-writing methods in transparent materials is to exploit nonlinear interactions between the laser pulse and the medium, in order to create localized permanent modifications in the bulk of the material. The modified regions exhibit different optical properties compared to the unmodified region, allowing for creation of buried optics inside the bulk, which can later be used for optical applications [5–7]. The electronic bandgap of a material determines the transparency, in terms of the wavelength range. When electromagnetic waves propagate through a medium, electrons in the medium start to oscillate and are excited through absorption and collisions. If the bandgap of the material is comparable to the photon energy, then the electron can be excited to the conduction band through linear absorption of a photon. For photons with energy lower than the bandgap, linear absorption is no longer possible, and the material is transparent at that wavelength. For silicon, the transparent regime starts at a wavelength of approximately > 1.2 μm, which is in the infrared regime of the electromagnetic spectrum.

In the transparent regime, if the intensity of the propagating laser light is high enough, electrons can be excited to conduction band through ionization mechanisms, such as two-photon absorption (TPA) or multiphoton absorption (MPA), depending on the wavelength and associated nonlinearities. Since TPA and MPA are nonlinear responses, they generally require high intensities in the transparent regime. Inducing

TPA, MPA or other ionization mechanisms such as avalanche ionization can result in a high amount of energy deposition in a confined space in the bulk of the material. In conjunction, plasma formation takes place, modifying the optical index temporally, which dynamically changes the absorption of the incident light. These set of responses result in a complex interaction. During the process, if the local temperature is high enough, material properties can be permanently changed at a narrow volume. The plasma formation has a delocalizing effect on the incident light, which may prevent further modification. However, at high enough intensities, the laser light can also undergo self-focusing, which is in direct competition to delocalization, resulting in modifications [15, 16]. The specific mechanism for modification depends on a range of factors, such as the intensity, timescale, material, and operating wavelength. The final result may include localized phase transitions such as amorphization (through rapid melting and solidification); or optical index change based on stress-strain effects.

1.1.2 State of the art in direct laser writing in silicon

Multiple studies have been carried out using lasers, with a focus on creating buried waveguides in silicon. Nejadmalayeri et al. demonstrated the earliest optical waveguides using a femtosecond laser [17]. However, the waveguides could only be fabricated very close to the Si-SOI interface, irrespective of the focusing depth inside the bulk. Subsequent efforts in forming fully buried modifications in the bulk of silicon were unsuccessful. The modifications formed only near the interface as shown in reference [17, 18], or were limited to the back-surface [14]. Kononenko et al. demonstrated the unusually high modification requirements, where subsurface structures were not created even with the extremely high pulse energy of 90 μJ, due to the high delocalization of plasma shielding [19]. Later, first laser-written functionality in silicon was achieved, without altering the wafer above or below the modifications [20–22]; with several studies confirming the initial results with both nanosecond and femtosecond pulses [24, 25]. The seminal paper on controlled 3D micro-fabrication in silicon by Tokel et al. in 2017 introduced a novel nonlinear laser lithography approach for 3D control in the bulk of the wafer, achieving high-aspect-ratio microstructures and large-volume covering laser-sculpted micro-structures [5]. These type of complex structures are termed "in-chip" optical elements or components, analogous to the well-known "on-chip" capabilities shown on other materials.

In-chip fabrication was achieved through nonlinear feedback mechanisms. A particularly useful example of this type of interaction is achieved by focusing the laser after the back surface of the sample; creating a reflected beam, which in turn initiates a feedback interaction between the two beams. The interaction results in the formation of controlled rod-like structures. Then, the rod-like structures can be used as building blocks for demonstrating various functional in-chip optical elements, such as Fresnel zone plates, gratings, waveguides, optical barcodes for data storage or in various in-chip holography applications [5–7]. Not surprisingly, multiple challenges remain in this new emerging field. A particularly important challenge is to improve the current $\sim$1 μm fabrication resolution. Can we push this further and introduce laser-based nanofabrication to the bulk of the wafer? Is it possible to create structures beyond the diffraction-limit? Following the introduction of such capabilities, would it be possible to create in-chip nano-photonics? Further, the effect of polarization has not been explored completely until now. Can we introduce laser polarization as a new control tool for in-chip laser lithography? We will attempt to answer these questions in the following chapters.

We get a strong clue from our current understanding of the formation mechanisms [5, 26, 27]. It is clear that the intensity distribution has a significant role in the formation of in-chip micro-structures. The beam type used in most studies is the Gaussian beam. The intensity profile of the Gaussian beam is confined to a small volume after focusing, due to its short Rayleigh length. Even with this limitation, creation of high-aspect ratio structures is already solved [5]. However, creating high-aspect-ratio structures, and simultaneously breaking the resolution limit of 1-μm seems challenging, and has not been possible so far. Reaching the nano regime has the exciting potential to introduce a new class of in-chip devices, e.g., nano-photonics components, including subwavelength gratings or photonic crystals. A promising approach towards this goal seems to be exploiting structured laser beams. The next section overviews the structured light and light-matter interactions using such beams, followed by the description of our methodology in the next chapter.

1.2 Structured laser beams and their potential for in-chip fabrication

Structured beams are a sub-class of optical fields which have inhomogeneous spatial distribution of beam parameters, such as amplitude, phase, and polarization [28]. The earliest laboratory-created structured laser beam with a helical structure was published in 1990 [29]. The interest in structured beams increased after the experimental demonstration of structured Laguerre-Gaussian mode carrying angular momentum [30]. Later, Harris et al. demonstrated that similar helical beam types exhibit characteristic interference fringes under an interferometric arrangement [31]. In both cases, the used beams were related to Laguerre-Gaussian modes, with the helical structure of the beams dictated by a particular azimuthal phase with a phase singularity along the optical axis, i.e., an optical vortex. Analogous studies on structured beams have developed into a wide field of research with extensive applications including, but not limited to, optical trapping [32–36], optical switching [37], quantum computing [38], and micromachining [39].

A special class of structured beam is the Bessel beam, first demonstrated by Durnin and Micheli in 1987 [40]. Higher order Bessel beams demonstrate a phase singularity similar to vortex beams, however, the smallest order or zero order Bessel beam does not exhibit this phase singularity. Bessel beams are of particular interest for laser material interactions in general, but for in-chip writing in particular. Bessel beams are part of a special class of beams, with inherent non-diffracting properties against defects in their path [41]. Zero order Bessel beams have a characteristic bright core at the centre, surrounded by weaker side lobes which can propagate over a very long distance without a loss in intensity [41]. Further, the intensity of the beam after focusing remains low along the optical axis until the onset of the high-intensity central core (defined as the Bessel zone), which allows strong spatial control.

Successful use of Bessel beams to fabricate high-aspect-ratio nano-channels in glass has already been demonstrated [42, 43]. In contrast, despite the potential of Bessel beams in nanofabrication in transparent materials, analogous studies in silicon failed to create any permanent index modification [44]. In this thesis, we exploit

Bessel beams, in order to demonstrate the first in-chip nanofabrication capability, with sub-diffraction precision. We achieve this using a combination of smart spatial modulation of zero order Bessel beam, in conjunction with a new observed effect, based on seeding of in-chip nano-structures from nearby preformed structures. In addition, we demonstrate polarization of the laser as a new control parameter for in-chip fabrication control. Finally, we demonstrate a proof-of-concept application of this approach, through the fabrication of the first in-chip volume Bragg-gratings with sub-micrometer feature sizes, and by experimentally confirming the diffraction efficiency as 85% at 1.55 μm operation wavelength.

Chapter 2

Methodology

We start by discussing the Bessel beam profile and how it can be created experimentally. An ideal Bessel beam is propagation invariant, with the zero order beams exhibiting a bright central core [41]. Finite Bessel beams can be experimentally generated by means of both physical and digital optics. The conventional method is to use physical optics, using axicons, a group of conical refractive devices. However, axicons come with a fixed conical angle, thus it is not possible to modulate the phase of the output beam. On the other hand, dynamic axicons can be created using digital optics, with holographic optical systems. Thus, diffractive systems such as deformable mirrors or spatial light modulators (SLMs) offer the freedom to modulate the beam, exerting control on the intensity of the core diameter and the length of the non-diffracting region. This non-diffracting region is also known as the Bessel zone. Bessel beams generated with SLM have a number of advantages over beams created with physical axicons. (i) In the former, the Bessel zone is reproduced more faithfully, compared to Bessel beams generated with round-apex axicon [45, 46]. (ii) The axicon angle can be dynamically changed in the former, whereas it is static in the latter. Thus, SLM generated Bessel beams are significantly promising for fully controlled laser structuring.

The Bessel zone of a zero-order Bessel beam is analogous to the Rayleigh length of a Gaussian beam. Both the core diameter and the Bessel zone length is critical in

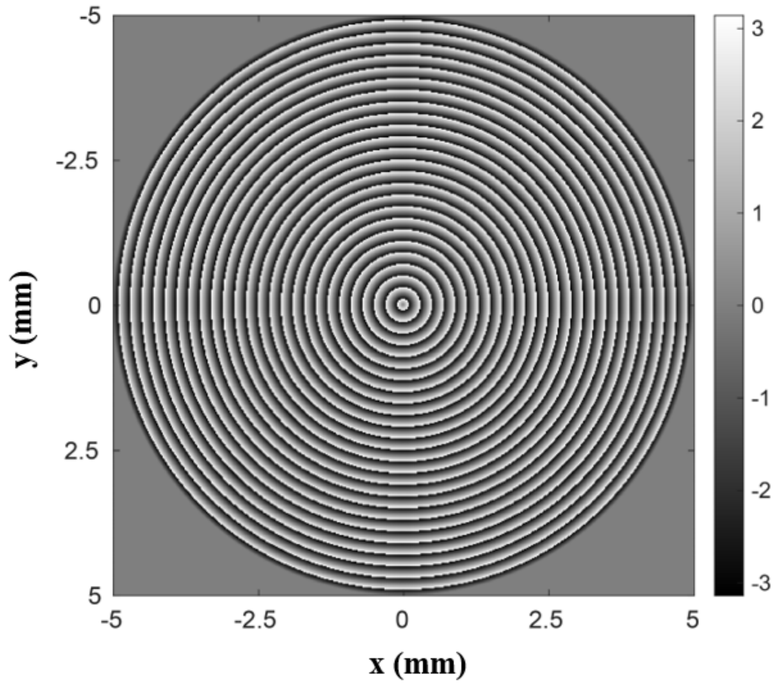

Figure 2.1: Computer generated hologram representing the phase mask for r_0 = 10.

achieving subsurface modification. In this work, a Gaussian beam is incident on an SLM, which then implements a Bessel pattern on the reflected beam. The radius of the incident beam w_0, the wave vector k, the diameter of the central core of the Bessel beam (d_B), and the length of the Bessel zone (Z_B) are related as follows:

$$Z_{\mathrm{B}} \sim \frac{w_{\mathrm{o}}}{tan(\theta)}, d_{\mathrm{B}} \sim \frac{2.4}{ktan(\theta)}. \tag{2.1}$$

One compromise arises here, smaller core diameters limit Bessel zone length, which would reduce the aspect ratio of modifications. This can be overcome by implementing a lens-axicon doublet by introducing an aspheric lens right before the sample. The approach effectively decouples the core diameter and the Bessel zone length, allowing adjustable core length, and constant core diameter. This made it possible to obtain high-aspect-ratio laser-induced structures and higher processing stability when scaling down different parameters like pulse energy.

In order to generate the Bessel beam, an SLM was used to modulate the phase of an incident Gaussian beam. The hologram is generated with a computer program (Holoeye OptiXplorer 2.8) implementing the particular phase pattern (phase mask) of the desired virtual axicon (Figure 2.1) on the SLM. The reflected beam takes on the desired phase, and a Bessel pattern is generated at the SLM output after free space propagation. The applied phase on the SLM had the profile:

$$\phi_{\mathrm{SLM}}(r) = e^{\pm\left(i2\pi\frac{r}{r_o}\right)} \tag{2.2}$$

A negative sign on the phase corresponds to a converging axicon, whereas positive sign corresponds to a diverging axicon. The r_0 parameter is linked to the cone angle θ such that,

$$r_0 = \frac{\lambda}{2\tan\left(\frac{\theta}{2}\right)} \tag{2.3}$$

In a converging axicon, Bessel zone starts before the focus, limiting control for subsurface writing. In contrast, for a diverging axicon, Bessel zone starts after the focus, enabling precise control over the positioning of the Bessel zone simply by adjusting the focusing parameters. In this case, the core forms in the far field, with a ring-like profile with modest intensity in the near field. This is instrumental in avoiding surface damage on the silicon wafer during fabrication of nanostructures. In this work, we exploited such a diverging axicon. The experimental setup will be described in section 2.2, following the beam characterization aspects in section 2.1.

2.1 Bessel beam simulation and experimental characterization

Fresnel diffraction expression and two dimensional fast Fourier transform algorithm were used to simulate the laser beam propagation after the SLM and focusing lens.

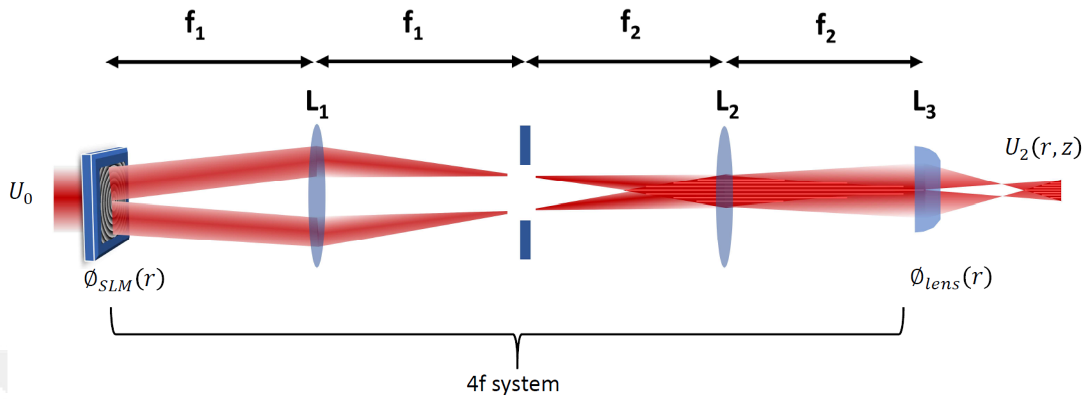

Figure 2.2: Schematic showing the propagation of the Bessel beam generated using the diverging-axicon and lens doublet. L_1 and L_2 serve as 4-f system that translates the SLM output to the aspheric lens (L_3) with a demagnification factor of 0.8.

According to the Fourier convolution theorem, the complex field distribution in the observation plane can be obtained by [47]:

$$U_2(r,z) = \mathscr{F}^{-1}[\mathscr{F}\{U_1(r,0)\}e^{ikz}e^{-i\pi\lambda z}|({f_x}^2 + {f_y}^2)|] \tag{2.4}$$

where, f_x and f_y denotes the spatial frequencies and U_1 (r,0) is the field distribution in the source plane and is expressed as:

$$U_1(r,0) = U_0\phi_{\text{SLM}}(r) \tag{2.5}$$

Here U_0 is the field amplitude and $\phi(r)$ is the phase pattern implemented on the SLM. The beam profile after the demagnification and focusing objective can be determined by considering the scaling factor and adding the lens phase pattern,

$$\phi_{\text{lens}}(r) = e^{-i\pi\frac{r^2}{\lambda f}} \tag{2.6}$$

in the diffraction equation. For the final simulation, considering both the SLM phase pattern as well as the focusing lens phase pattern, the expression takes the form:

$$U_1(r,0) = U_0\phi_{\text{SLM}}(r)\phi_{\text{lens}}(r) \tag{2.7}$$

When the field distribution is known, the intensity distribution in the observable plane can be calculated from the expression:

$$I_2(x,y) \propto |U_2(x,y)|^2 \tag{2.8}$$

In order to generate the Bessel beam, a phase mask with the positive phase profile is applied. The phase corresponds to a diverging axicon, with the output beam having a ring shape and Bessel beam profiles in the near and far-field, respectively.

The experimental setup includes a diverging axicon plus a focusing lens to generate Bessel beams, as well as the 4-f system for beam scaling, filtering and imaging. A schematic of the generated beam along with the associated lens systems is given in Figure 2.2. Simply by changing the r_0 parameter in the phase profile, Bessel beam profile can be changed, analogous to beam profiles created with physical axicons of different cone angles. The final lens effectively increases this angle inside the high-index wafer. Thus, we exploit the final "zeroth order Bessel function of the first kind" for micro-/nano-structuring in silicon. We choose to r_0 in terms of pixel numbers (e.g., r_0=10 pixels correspond to r_0=10×20 µm and cone angle $\theta = 0.43°$.)

For optical characterization, the output beam was imaged and the intensity was measured along the optical axis with increments of 2 µm using an InGaAs camera (ARTCAM-03ITNIR) providing 2D intensity profiles. Figure 2.3 shows the experimental 2D intensity profiles of a Bessel beam in air (r_0 = 10). The corresponding 1D intensity profiles are given in Figure 2.4, for both simulated and experimental beams are. The beam characterization thus confirms that we have a zero order Bessel pattern at the output of the SLM-lens doublet.

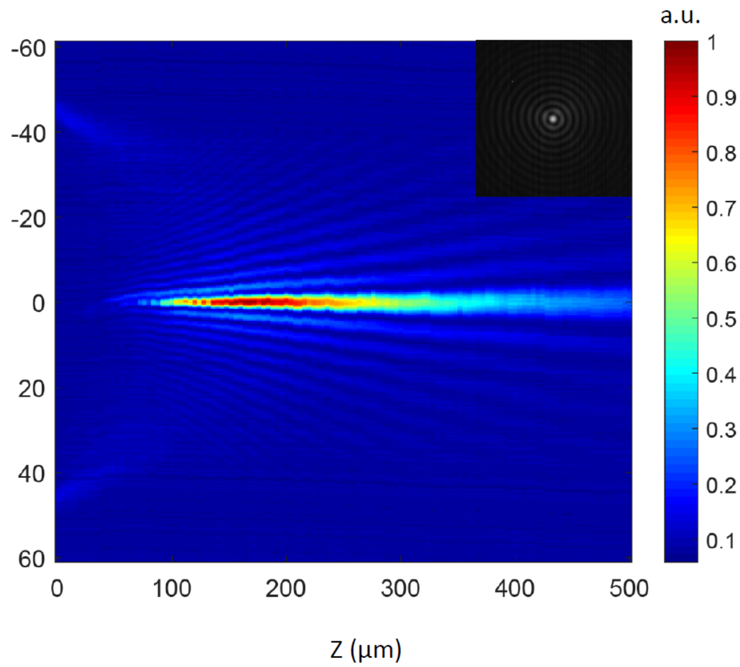

Figure 2.3: The experimental intensity profile in x-y and x-z planes measured in air for r_0=10 after the focusing lens and along beam propagation direction. The inset shows the cross-sectional view (x-y plane) at maximum intensity point, imaged with an InGaAs camera.

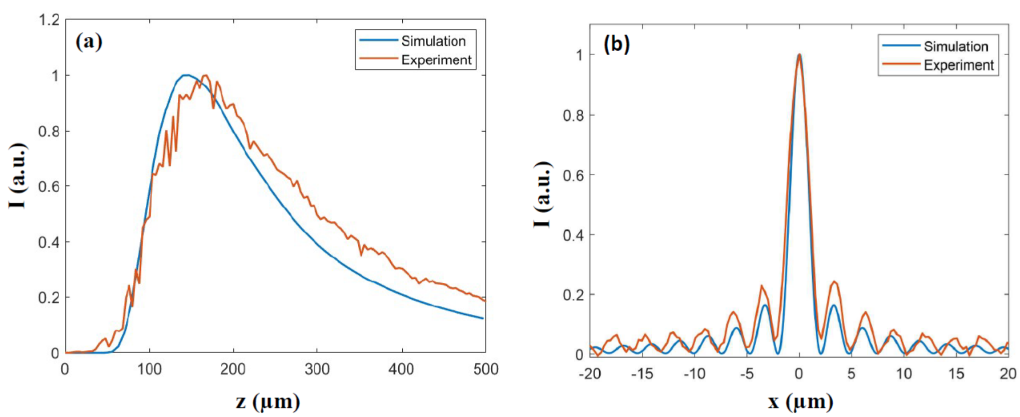

Figure 2.4: Beam characterization with 1D profiles. a) Comparison of simulated and experimental intensity profiles along laser propagation in air after the focusing lens. b) Comparison of the intensity in the transverse plane, at the maximum intensity point along laser propagation direction.

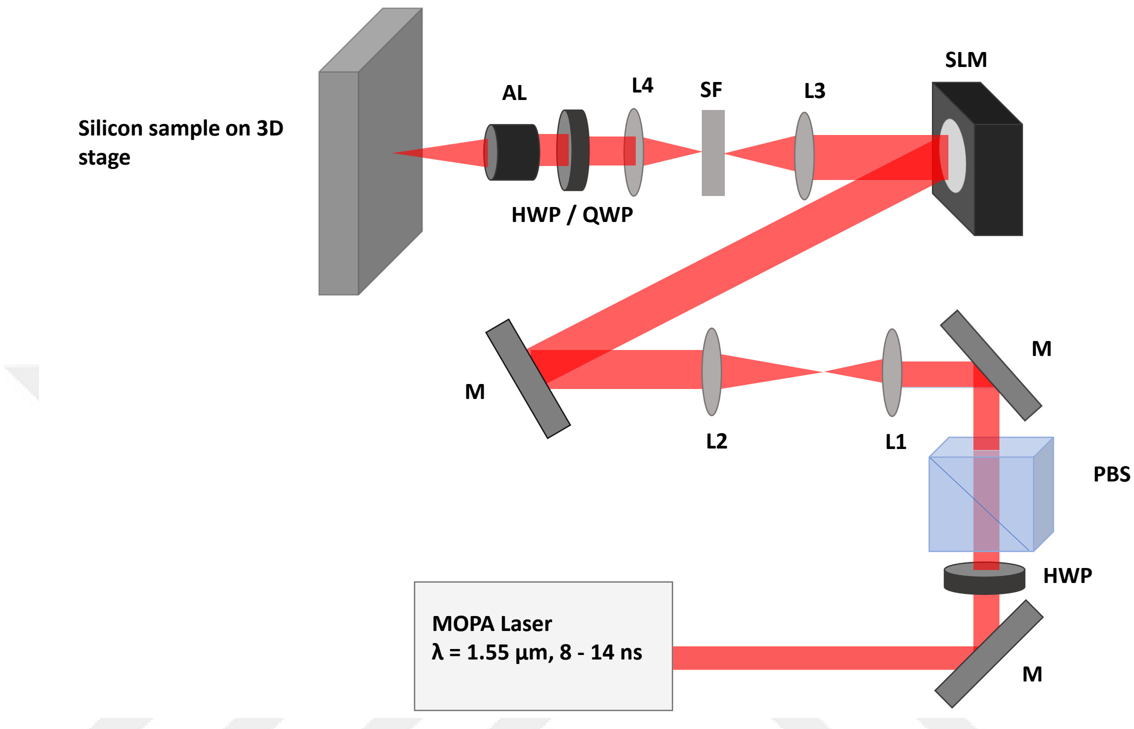

Figure 2.5: A schematic of the experimental setup for direct laser writing of silicon.

2.2 Experimental setup

The laser setup for in-chip fabrication using Bessel beams is given in Figure 2.5. A custom built all-fiber-integrated master oscillator power amplifier system is used as light source. This laser produces pulses in the range of 5 - 30 ns with maximum power of 6 W at 150 kHz repetition rate at 1.55 µm wavelength. The power and polarization of the laser are controlled by a set of half wave plates (HWP) and polarization beam splitters (PBS). Additional control over the polarization is achieved using with a HWP or quarter wave plate (QWP) befoxpand the beam diameter to achieve the most efficient incident spot size on the SLM. The focal depth of L1 and L2 are f1 = 15 mm and f2 = 35 mm respectively. For this work, a Hamamatsu liquid crystal on silicon SLM with 792 × 768 resolution and 20 µm pixel size is used. The incidence angle is kept below 10 degrees, and a blazed grating is used on the applied phase mask to separate the diffraction orders before the last focusing lens. A telescope system (L1 and L2) is used to expand the beam diameter to achieve the most efficient incident spot size on the SLM. The hologram surface is tilted to align the +1 order along the optical axis. All other diffraction orders are eliminated using a spatial filter. A 4-f system with f1 = 12.5 cm and f2 = 10 cm is set after SLM to translate the beam shape on the SLM with the de-magnifying factor of 0.8 to the focusing lens aperture. Finally, an aspheric lens (f = 4.5 mm and NA = 0.55) is used to focus the beam inside silicon for controlled micro-/nano-fabrication. For accurate positioning of the beam in silicon, the wafer was mounted on a high-resolution computer-controlled three-dimensional stage (Aerotech ANT95-L-Z).

We generated various Bessel beams and performed a multitude of experiments to control the feature size of subsurface modifications, among other parameters. The laser-writing was carried out with transverse and longitudinal scanning configurations. In the transverse mode, typically a raster scan was carried out for characterization, and then for fabricating in-chip optical devices such as nano-gratings (see chapter 4). We label the z-axis as laser propagation direction, and the sample is scanned along y-axis, on the x-y plane. The subsurface structures fabricated in this modality were confined in **1 dimension**, in the x-axis, perpendicular to the laser propagation direction (Figure 2.6, left). Thus, by exerting control on the minimum thickness of the structures along x-axis, we demonstrate 1D control of the laser written nano-structures.

In order to push our freedom for nano-scale structuring, we modified the wafer without any planar scan, using longitudinal modality (Figure 2.6, right). In this mode, the sample is scanned along the laser propagation, creating an elongated cylindrical structures with adjustable length. These structures are confined in both x and y-axes (2-D confinement), and for nano-fabrication, will require a pre-formed seed to form, as we will describe in chapter 3.2.

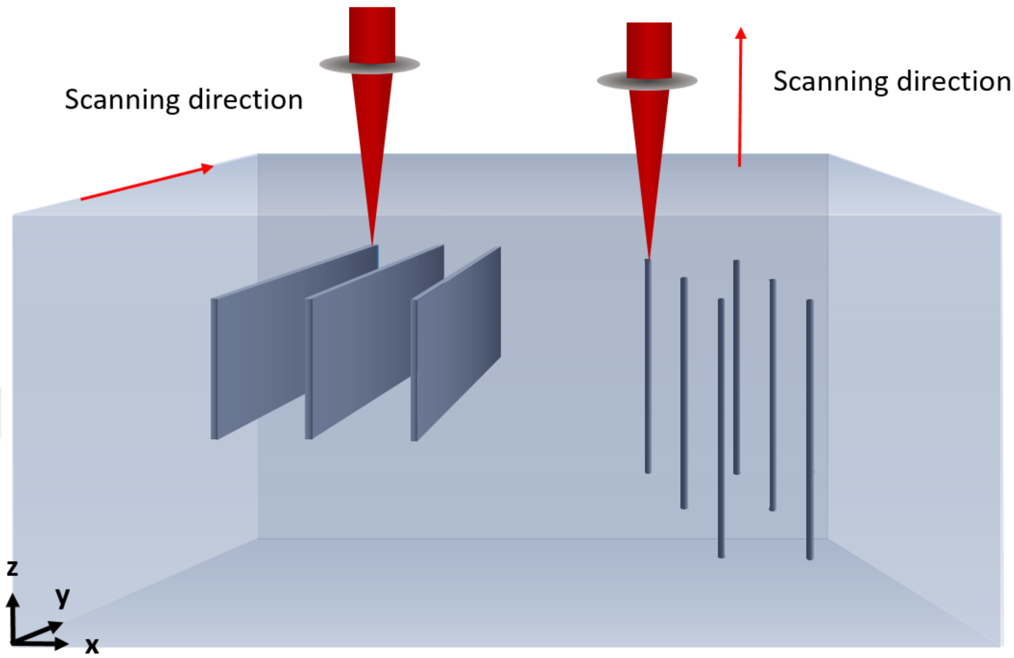

Figure 2.6: Schematic shows the transverse writing modality (left) and longitudinal writing modality (right) for in-chip structures.

2.2.1 Experimental methods for characterization

In-chip structural changes are initially evaluated with a home-built infrared transmission microscope (ITM) consisting of a broad-spectrum halogen lamp and an electron-multiplying charge-coupled device (EMCCD) camera (Andor, Lucas). The resolution of the ITM is limited to 1 μm, so for precise measurements of the subsurface structures, a scanning electron microscope (SEM) is used. In order to image the structures confined in 1D with the SEM, the sample is cut from the middle with a diamond-tip cutter and the cross-section (x-z plane) is imaged under SEM revealing structure lengths and feature sizes. The 2D-confined structures are harder to find inside the bulk, and cannot be resolved with ITM, thus we had to depend exclusively on the SEM for locating and imaging.

2-D confined structures were acquired from the x-y plane. In order to allow this, we carefully polished the sample from the surface and chemically etch at the desired plane, before acquiring the SEM images. The selective etching was needed in order to reveal the nano-structures. These structures were extended along z-axis (scanning longitudinally). By adjusting the initial position of the Bessel zone and the scanning length, we were able to extend the structures throughout the whole sample thickness without damaging the front and rear surface of the silicon sample.

2.2.2 Sample type

Primarily two types of samples were used in the experiments. A majority of the 1D experiments were conducted with 1 mm thick Si sample with orientation <100>, with resistivity = 5-15 Ω.cm. The majority of the 2D experiments were conducted with 1 mm thick Si sample with orientation <111>, with resistivity = 1-10 Ω.cm. The different sample types were used interchangeably based on availability. The two sample types only differed in the crystallographic orientation, with slight difference in the resistivity range and we did not observe any significant difference between the results obtained with the two sample types.

2.2.3 Sample preparation for imaging: polishing

Polishing was an integral part for imaging the 2D-confined structures as we needed to reach the buried structures for selective chemical etching. The samples were polished using the chemical mechanical planarization (CMP) technique, utilizing an automatic polisher (ALLIED-MULTIPREP) and a series of diamond lappings with different roughness. The table below presents the general parameters used in the CMP process. Polishing time and certain parameters were adjusted depending on the polishing depth and surface quality requirement. For polishing, the sample is first attached to a small disk using an adhesive polymer which was first melted and re-solidified, acting as a glue that attached the sample to the disk. The initial width of the sample and glue layer is then measured using a micrometer. The machine is then switched on and the disk is attached to the machine such that the sample is facing downwards towards the rotating platen. A diamond lapping is placed on the plated and the sample is lowered until the surfaces touch. The sample is further lowered by the amount that needs to be polished. It is better to adjust the sample position and lower it gradually over time to avoid breaking the sample. Two additional micrometer scale sensors are used to ensure accurate positioning of the sample. Different lapping sizes are then used to first etch the sample from the desired surface uniformly (hard polish), then to polish and smoothen the surface to reach high reflectivity (soft polishing).

Table 2.1: Parameters for the CMP process.

No. of steps	Lapping size (µm)	Platen rotation speed (rpm)
1	30	200
2	15	150
3	9	100
4	3	50
5	1	40

2.2.4 Sample preparation for imaging: selective chemical etching

The selective chemical etching process is based on the oxidation of silicon and its immediate dissolution [48]. The etching solution consisted of 0.05 M of $Cu(Cu(NO_3)_2)$, 10 M of hydrouoric acid (HF), 4 M of nitric acid (HNO_3) and 3.5 M of acetic acid (CH_3COOH). The recipe was previously developed, with its effectiveness demonstrated in [5] for laser assisted chemical etching of silicon. The etchant served to selectively remove the laser irradiated zone. The HNO_3 serves to oxidize the laser irradiated zones while the HF removes the oxidized silicon [49, 50]. The CH_3COOH dilutes the reactance concentration. $Cu(Cu(NO_3)_2$ is used to enhance selectivity of the etchant due to its low activation energy [51, 52]. The etching process was carried out in a cleanroom environment in a fume hood. HF is a highly corrosive material and must be handled with absolute care.

Chapter 3

Results and Discussion

In order to see how structured Bessel beams can be exploited for in-chip micro-/nano-fabrication, we explore how the phase modulation changes the spatial field distribution. The simulations in Figure 3.1a show Bessel zone forming in air, after the focal plane of the lens, assuming three r_0 values. We normalized the intensity with respect to the beam with largest r_0. We observe that, the peak intensity along the propagation direction decreases as r_0 is reduced. Further, with reducing r_0, the location of the peak intensity moves away from the focal plane, along the optical axis. This indicates that the modifications can be expected to form at different points, even when using the same focusing lens and with no sample translation. In addition, the Bessel zone length increases for smaller r_0 values, extending well over a few hundred micrometers in air. All of these parameters need to be considered for finding appropriate conditions for in-chip fabrication. In particular, there is a balance between modification length and extending Bessel zone for smaller r_0 values.

Since we are interested in pushing the fabrication limit, we also evaluate smallest experimental r_0 values in the simulations. Figure 3.1b shows the corresponding simulated intensity distributions measured on the transverse plane, at the peak intensity position along the optical axis. For smaller r_0 values, the core diameter remains approximately constant and is about 3 μm. We can get an estimation on the general trend for feature size, assuming a simple (and arbitrary) nonlinear modification threshold.

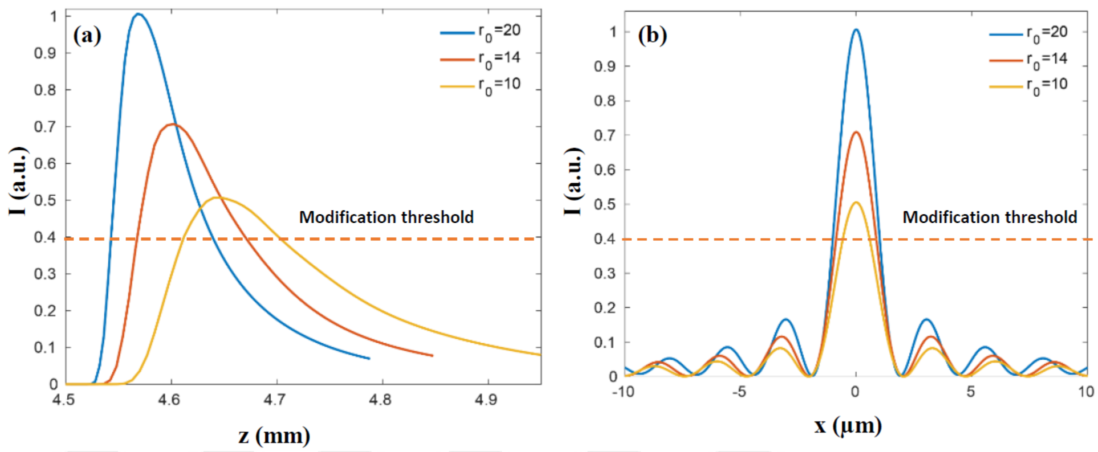

Figure 3.1: Simulations showing the laser intensity profile for different r_0 values. (a) Intensity along the laser propagation direction. (b) Intensity on the transverse plane at the maximum intensity along the optical axis. z = 4.5 mm corresponds to the focal plane of the lens.

From Figure 3.1b, we would expect to create smaller feature sizes with smaller r_0 values, while preserving the input pulse energy. This is due to the smaller volume remaining over the modification threshold for smaller r_0 values. In practice, due to coupled nonlinearities, this is a highly complex system, however this simple model is found to be a valuable guide in our experiments. Pulse energy and polarization are further parameters for advancing control. Hence, with our setup and with judiciously chosen set of parameters, we can achieve tunability of the Bessel zone length and diameter for fabrication. Next, we will explore the use of these parameters for in-chip fabrication.

3.1 In-chip micro-and nano-structures with 1-D confinement

Here, we demonstrate the first highly-controllable Bessel-written micro-and nano-structures in silicon formed with 1D confinement (corresponding to planar formations), followed by a systematic investigation of their positioning within the wafer. In order to reliably create high-aspect-ratio structures, it is important to determine the best parameter set for the initiation of modifications. Our simulations show that, for smaller r_0 values, the length of the Bessel zone increases, while the peak intensity drops. This behaviour predicts a change in the formation location with decreasing r_0 values, as illustrated in the schematic given in Figure 3.2. This shift is expected without even moving the sample or the laser with respect to each other, but simply by changing the phase on the SLM.

Our experiments revealed that larger r_0 values ($r_0 > 30$) tend to produce structures similar to those created with Gaussian beams, forming with larger feature sizes. This is expected, due to their large effective core diameter and shorter Bessel lengths. We then moved to smaller r_0 values for a systematic analysis of structure formation and positioning. We performed raster scans with the same pulse energy, preserving horizontal polarization. We also selected the focusing condition such that Bessel zone remains within the 1-mm thick sample, for even the smallest r_0 value (r_0 = 6). The pulse energy is kept above threshold for all experiments.

Figure 3.3 shows comparison of experiments and simulations, both corresponding to the onset of the Bessel-written structures in Si. The position of structures was estimated from the simulated intensity profile obtained for different r_0 values in air and then estimating the position in silicon with the simple assumption that modification is initiated immediately at the onset of the Bessel zone in Si. This is a reasonable assumption since the pulse energy is kept high for all experiments. These results indicate that decreasing r_0 values moves the onset of Bessel zone towards the exit surface (Figure 3.2), and provided a good match between the experiments and simulated results (Figure 3.3). This indicates that it is possible to estimate the position of the Bessel-beam written modifications based on the phase of the beam. This also raises the question of whether one can estimate the length of structures. In order to carry out such experiments, thicker samples would be required, to completely remain inside the wafer for low r_0 values. However, we found that it is possible to optimize the structure length by keeping the phase constant and adjusting power, depth, and the numerical aperture of the aspheric lens.

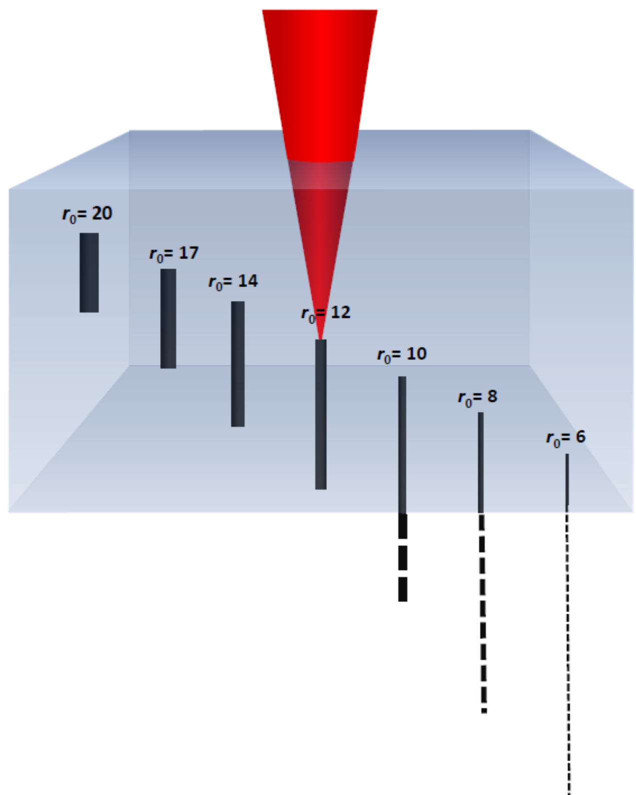

Figure 3.2: The schematic illustrating how the positions of the modifications move in Si with r_0, without changing the sample or laser position, but simply with changing the phase on the SLM.

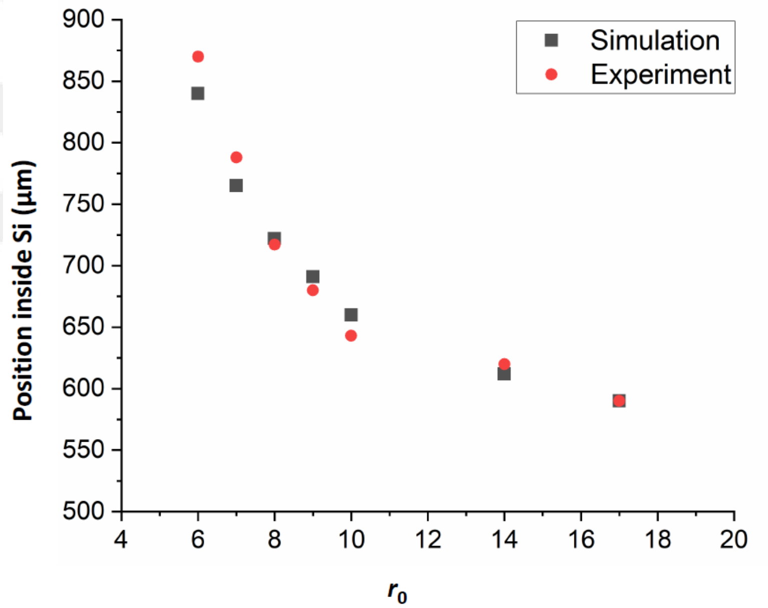

Figure 3.3: Comparison of experiment and simulations for the onset of modifications in Si with changing r_0, but without changing the sample position or the focusing lens with respect to each other. Laser parameters are, Pulse energy = 6.3 µJ, scan speed =1 mm/s, pulse width = 8 ns, with a silicon sample with orientation $<100>$, that was 1 mm thick with resistivity = 5-15 Ω.cm. Polarization is parallel to scanning direction.

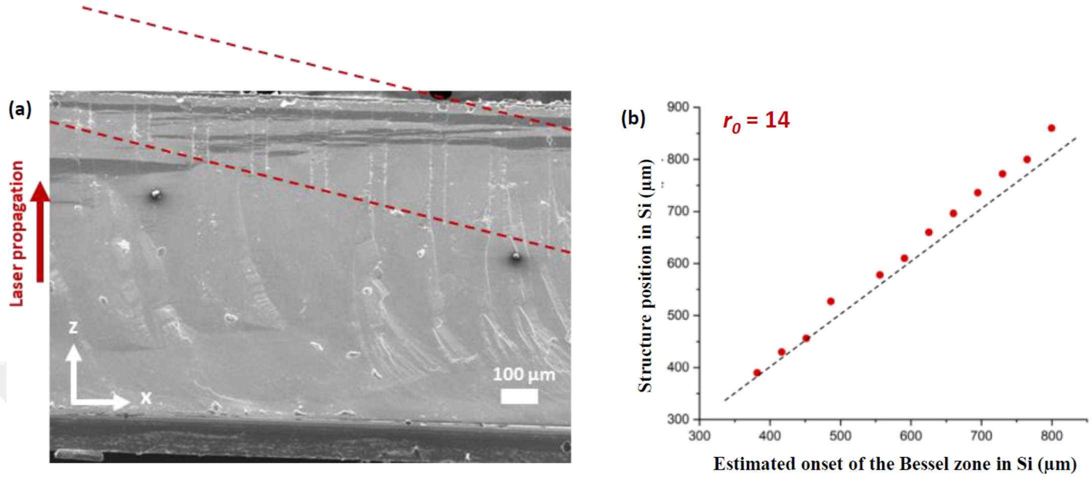

Figure 3.4: (a) SEM image of pair formations at different depths, created by physically changing the focusing depth of the laser in Si. Pulse energy = 6.3 µJ, r_0 = 14, scan speed =1 mm/s, pulse width = 8 ns, with a silicon sample with orientation <100>, that was 1 mm thick with resistivity = 5-15 Ω.cm. Polarization is kept parallel to scanning direction.The dashed lines demonstrate the expected shift and extension of the modifications if the sample was thicker. (b) The figure shows that the structure position can be predicted by simply assuming that the modification is initiated at the onset of the Bessel zone, for large pulse energies.

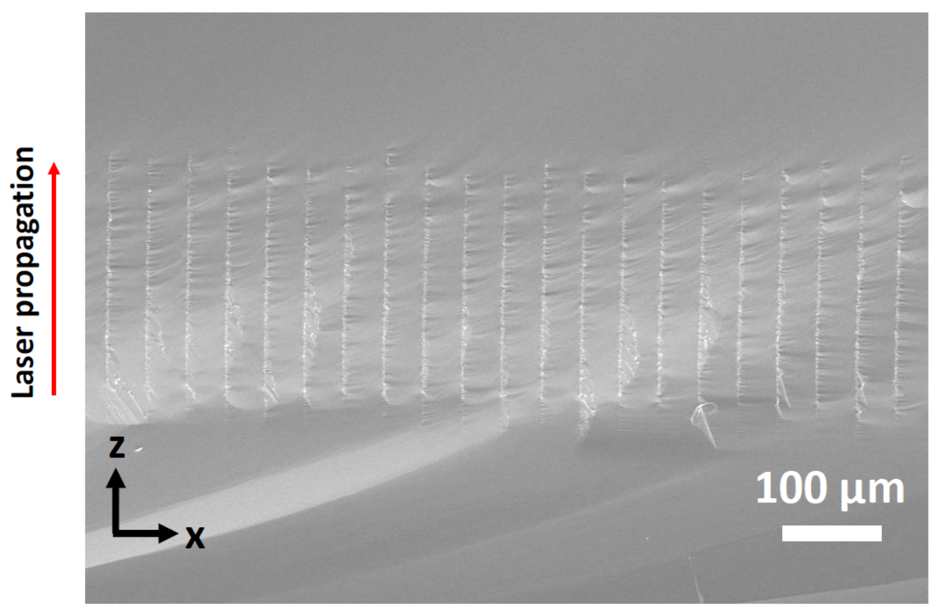

Figure 3.5: SEM image of the silicon cross-section showing fully buried Bessel written microstructures inside silicon, created with a pulse energy = 6.3 µJ, r_0 = 20, scan speed =1 mm/s, with a silicon sample with orientation <100>, that was 1 mm thick with resistivity = 5-15 Ω.cm. Polarization is parallel to scanning direction.

We then investigated how much control one can exert on the formation and position of the structures by physically varying the focusing depth inside silicon. We choose r_0 = 14, and use horizontal polarization along scanning direction. The pulse energy was set to 6.3 μJ, with the scanning speed of 1 mm/s, and initial depth of 416 μm from the laser entrance surface. The position of the sample was adjusted for every pair of linear scans, such that the focus of the laser is shifted by 34 μm in Si (10 μm in air). We observe that the onset of formations shift in accordance to the change in focus, as given in Figure 3.4a. Figure 3.4b shows the position of modifications versus the onset of the Bessel zone in Si, according to the simulated positions and taking into account the focusing depth in Si. We obtained a near x = y curve, as shown in Figure 3.4b, validating the assumption that the onset of Bessel zone is a good indicator for the position of structures.

With our understanding of the influence of phase and focusing conditions on the formation and positioning of the Bessel written microstructures, we were able to reliably form high-aspect-ratio Bessel-beam written modifications virtually anywhere inside silicon (Figure 3.5b).

Next, with the demonstrated control over the fabrication of in-chip microstructures with Bessel beams, we will focus on the fabrication of the first in-chip submicron structures. We started by decreasing the central core diameter by decreasing the pulse energy and r_0 value. We observed that experiments conducted with r_0 = 10 have given the most reliable results. Smaller r_0 values require higher power due to the reduced peak intensity, which can make it difficult to determine the exact fluence necessary to induce submicron modifications. Thus, r_0 = 10 demonstrated higher sensitivity to the pulse energy, allowing us to control the thickness of the structures with one-dimensional confinement over a larger parameter range, and finally crossing the submicron barrier for the first time in Si. Figure 3.6 shows the first laser-written nanostructure in Si, achieved with r_0 = 10, with a pulse energy of 4 μJ and with circular polarization. A detailed analysis of the influence of polarization and laser power for 1D confinement will be presented in sections 3.2 and 3.3 respectively.

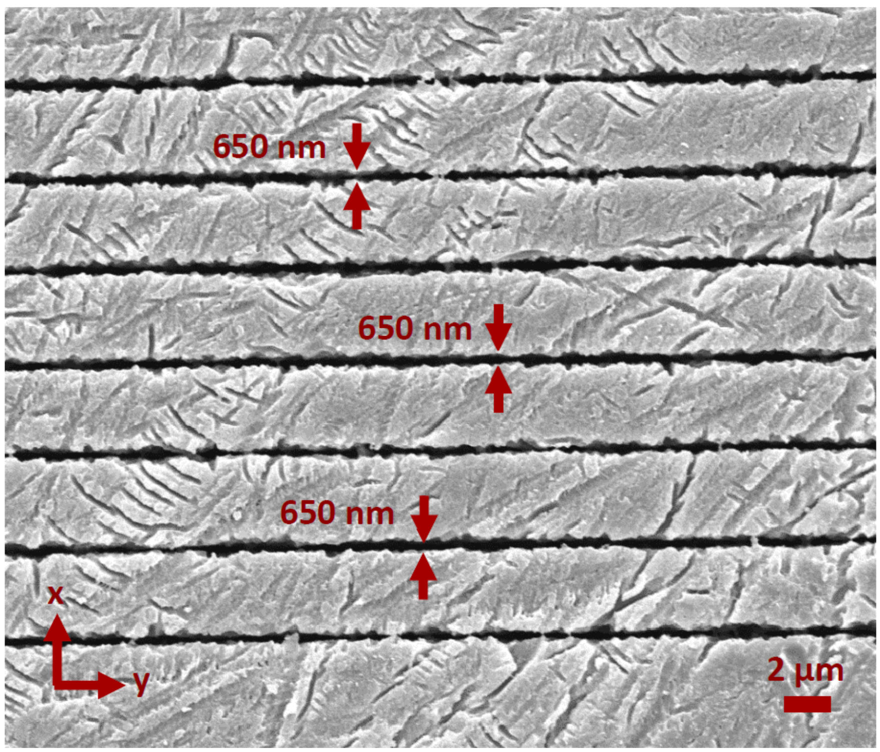

Figure 3.6: First demonstration of laser-written nanostructures deep inside silicon, polished from the top plane and etched for 30 seconds to reveal the modified areas. created with a pulse energy = 5.7 µJ, r_0 = 10, scan speed =1 mm/s, with a silicon sample with orientation $<$100$>$, that was 1 mm thick with resistivity = 5-15 Ω.cm. Polarization is circular. The structures are actually planar (one-dimensional confinement), but are imaged from a planar cross-section.

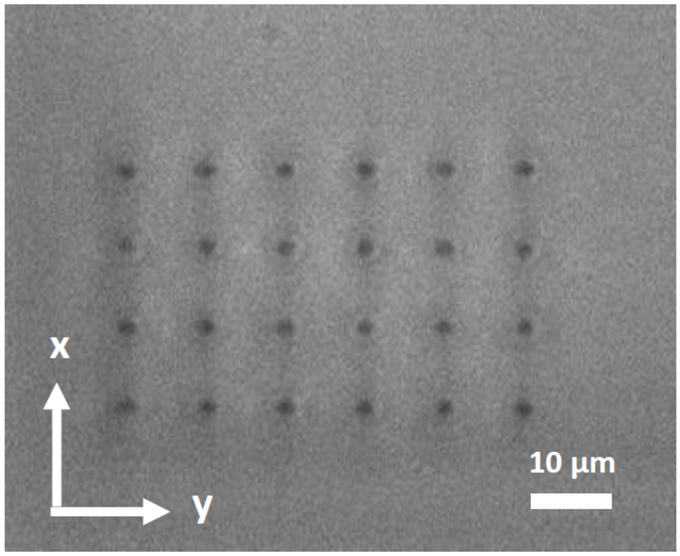

Figure 3.7: 2D cross sectional infrared transmission microscope image of an array of cylindrical modifications fabricated inside silicon, using circular polarization. The pulse energy was 10 µJ, and $r_0 = 14$.

3.2 In-chip micro- and nano-structures with two-dimensional (2D) confinement

Here, we demonstrate two-dimensional control (i.e., 2D confinement) at the micro- and nano-scale inside silicon. We start with 2D confined microstructures, and then move on to the nanoscale formations. In order to achieve the former, we switched from transverse-writing modality to longitudinal modality, where the laser is scanned along the laser propagation direction, creating elongated, cylindrical modifications along the optical axis (Figure 3.7). Similar results had been achieved with Gaussian beams at the micro-scale [53], however, the length of the structures along the optical axis may be limited by the length of the Rayleigh length. More importantly, Gaussian beams have larger feature sizes when directly focused in Si, due to diffraction. Bessel beams, on the other hand, allow a better tunability in the structure thickness. We created an array of 2-D confined microstructures that elongate along the laser propagation direction. When imaged at a plane, these are revealed as "micro-dots", each of which corresponds to a single laser scan (Figure 3.7). In order to create the second "dot", the laser is blocked, while the sample position is adjusted, such that the focal depth of the laser was inside Si, then, the laser is unblocked and the longitudinal scan is performed. The procedure is repeated for consecutive modifications. Figure 3.7 shows an infrared transmission microscopy image of a 2D micro-array created in Si.

Next, we move on to our primary objective, to reduce the cross-section of the modifications below the 1 μm level, effectively demonstrating 2D control at the nanoscale.

With our understanding of the field distribution of the Bessel beam, we hypothesized that we could scale down the diameter of the "dots" by decreasing the r_0 parameter and/or scaling down the pulse energy. However, we made the following observation: although microstructures could be created by longitudinal scanning or even by exposing the sample to the laser without scanning, we found that the structures stopped forming completely as we decrease the pulse energy or the r_0 parameter to the range that had been used in the creation 1D nanofabrication that was shown in the previous section (i.e. $r_0 \leq 10$). Surprisingly, this was true even for high-pulse energies for $r_0 \leq 10$, indicating that transverse scan had something unique that is not there in the longitudinal case. Perhaps previously formed structures were helping to seed the next structures. We tested this hypothesis by using previously-written 1D-confined structures (planes) created with transverse modality that will act as a "seed" for creating 2D-confined nano-structures (nano-lines). In order for this to work, the seed should be in close proximity to the target area (Fig. 3.8). This was confirmed in the experiments, where the 2D nano-line stopped forming as we move away from the seed line. The 2D-confined nano-lines were written in very close proximity of the pre-formed plane, within a range of 1-2 μm, as illustrated in Figure 3.8.

To this end we utilized the longitudinal writing modality and we extended the length of the structures along the wafer thickness by moving the sample in the laser propagation direction. To expose these subsurface structures, we polished the sample laterally and etched chemically. By adjusting the initial position of the Bessel zone inside sample and the scanning length, we extended these structures throughout the entire sample thickness without damaging either the front or back surface of the silicon wafer, which then allowed us to polish the sample from either surfaces to reach the structures. This also makes it possible to utilize the array of cylindrical

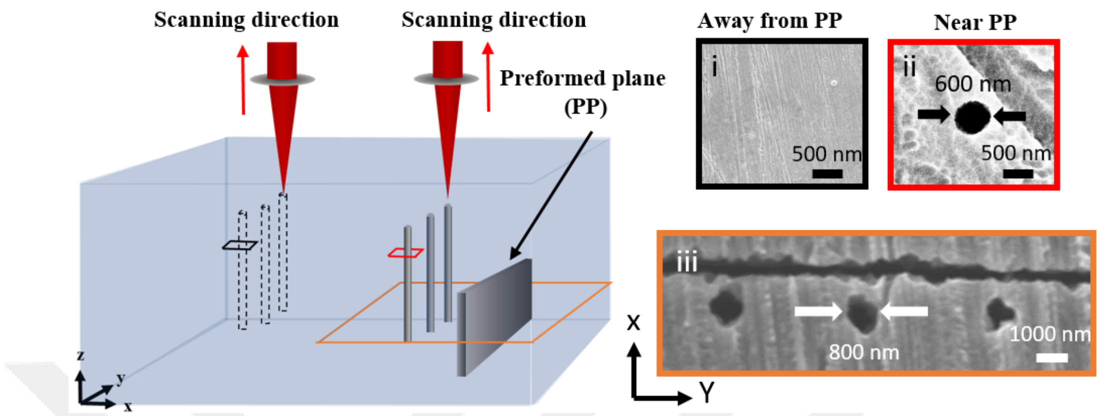

Figure 3.8: Schematic demonstrating the seeding effect for creation of 2D confined nano-lines. The formation of the nano-lines are due to preformed (nano or micro) in-chip structure, acting as a 'seed'. The range of this seeding effect is ≈ 1 µm. The insets show SEM images of polished and etched samples at different depths. The SEM image with the black border shows that nano-lines do not form at all, in the absence of a seed. The SEM image with the red border shows an individual 2D confined nan-line, imaged at a particular depth. The SEM image with the orange border is recorded at a deeper plane, simultaneously capturing the seed and the 2D-confined nano-dots. The seed is made with r_0 = 10 while the 2D dots are made with r_0 = 7. The etching time was 30 seconds.

nano-structures at a depth where the seeding lines are absent, as demonstrated in Figure 3.10. We can arrange these structures in an arbitrary architecture to design large scale area with submicron feature size. Figure 3.10 shows etched micro-and nano-dots created with proximity seeding while utilizing $r_0 \leq 10$.

While the dots do not form away from the seed, once it forms (in the proximity of a seed), it can easily be elongated along the optical axis, meaning that the 2D structures could be extended throughout the bulk of the sample simply by scanning longitudinally. Although we observed this seeding effect empirically, more research is needed to explain how this effect emerges. However, this already provides a powerful fabrication capability.

Imaging 2D-confined nano-lines: A particular challenge in pushing the resolution in the bulk of an opaque wafer is imaging nano-structures. We could verify the formation and position of the structures with infrared transmission microscope, however we were not able to resolve them with the 1 µm resolution of the infrared light,

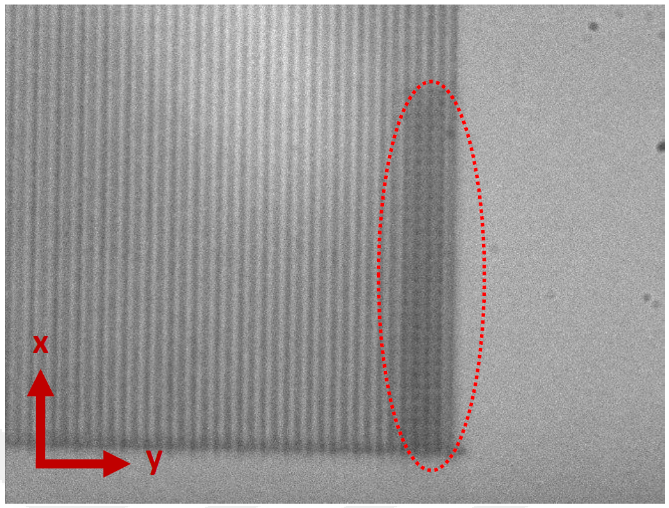

Figure 3.9: Optical transmission image of Si bulk showing both the 1-D confined seed structures (continuous lines on the left) and the formation of the discontinuous 2D-confined array (red-dashed line). The 2D nano-array cannot be resolved at this wavelength.

as indicated with the red-dashed curve in Figure 3.9. Unlike 1D confined structures, 2D-confined nano-lines also do not allow direct imaging with SEM. Thus, we needed a new approach for imaging the samples under SEM for accurate measurements.

To this end, we use the longitudinal writing modality and extended the length of the structures along the wafer thickness, simply by moving the sample in the laser propagation direction. To expose these subsurface structures, we polished the sample laterally and etched chemically. By adjusting the initial position of the Bessel zone inside sample and the scanning length, we extended the structures throughout the entire sample without damaging either the wafer surfaces. Then we polish the sample from any surface to reach the buried structures. This approach makes it possible to image the array of 2D-confined nano-structures at any depth, including where the seed structures are absent, as shown in Figure 3.10. We can arrange these structures in an arbitrary architecture to design large-scale area with submicron feature size. Figure 3.10 shows etched micro-and nano-dots created with proximity seeding while utilizing $r_0 \leq 10$.

The minimum achievable diameter of the nanostructures with circular polarization was found to be approximately 600 nm (with r_0 = 6), while we expect to achieve

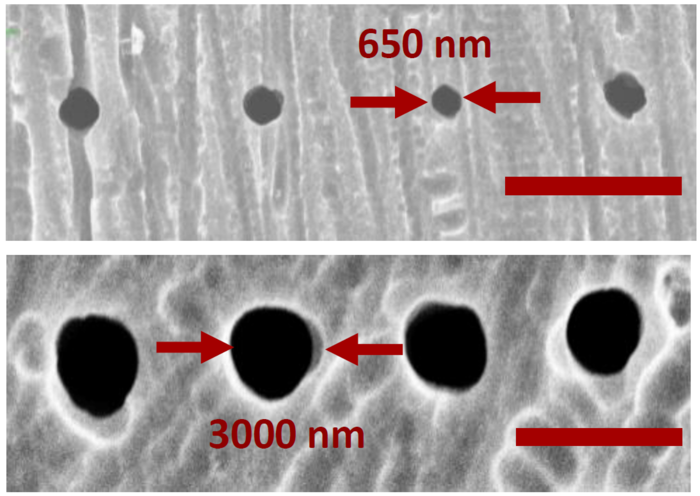

Figure 3.10: SEM image of 2D-confiend in-chip micro-structures (r_0 = 10) and nanostructures (r_0 = 6), revealed with polishing and etching (30 seconds). In both images the scale bar is 5 μm.

smaller structures with better optimization of the experiments. Characterizing 2D structures poses some inherent difficulties, as one needs to go through multiple post-processing steps, such as polishing and etching, before imaging. This makes it impossible to analyze the exact shape and size of the structures before post processing. It is important to note that for a brief etching time, as we use after the experiments, we did not notice any significant increase in feature size for 1D-confined structures. It is also reasonable to assume that the situation is similar for 2D-confined structures. However, the architecture of 2D structures may be somewhat affected by mechanical polishing.

We also found that the 2D-confined structures written with linear polarization have shown more consistency in shape and size after post processing. A detailed analysis of the effect of polarization is presented in the next section. Nonetheless, since the post processing steps are primarily for characterization purposes, it is reasonable to assume that un-etched, unpolished structures can be efficiently used for nanoscale optical applications.

Although we demonstrate the first laser-written in-chip 2D nanostructures, even better control may be achieved with the optimization of parameters, such as, phase, number of pulses, power and scanning length/time. It is important to note that future work will also benefit from a deeper understanding of the formation physics and, optical and material properties of the structures. Our experiments with 1D and 2D architecture had significantly improved our understanding and capabilities based on laser-silicon interaction at the nanoscale. Due to the unique geometry of 2D structures, we could investigate the effect of polarization on the formation of these structures, which ultimately lead to our discovery of a new regime of laser writing in silicon, the sub-diffraction regime. The following sections discuss the effect of polarization on the architecture of the laser written structures, and how that can be utilized to break the diffraction limit inside silicon.

3.3 Effect of polarization (architecture)

So far we have demonstrated nanofabrication in silicon with both 1D and 2D architectures with approximately 650 nm resolution, primarily with circular polarization. In order to reduce the feature size of the laser-written structures, we take a deeper look at how polarization affects them. Polarization refers to the confinement of the electric field oscillations during propagation. In linear polarization, the field is confined to a single plane along the propagation direction. In circular polarization, the linear components making up the beam have a phase difference of π/2. Previous studies did not go deeper on the effect of polarization, however, a significant polarization effect was not observed with Gaussian beams [54]. The new experiments exploiting Bessel beams indicate a distinct dependence of the structure size on polarization, for any given power and focusing condition.

In order to test the effect of polarization on laser-written structures, we carried out a systematic study by fabricating an array of 2D-confined nano-dots using different polarizations. We used r_0= 8, with the pulse energy of 3.7 ± 0.3 μJ, with four different polarization settings, i.e., horizontal polarization (p-pol), vertical polarization (s-pol), circular polarization, and polarization at 45° with respect to the horizontal plane. We observed a remarkable change in architecture of the structures (Figure 3.11). The laser-written nano-structures were oblique, confined to a narrower volume, perpendicular to the direction of the polarization.

A key observation from this experiment was that, the minimum thickness in a particular direction was significantly smaller for linear polarization (350 nm) compared to that of circular polarization (800 nm), under otherwise the same parameter set. This observation indicates that even smaller thicknesses could be achieved for novel applications with linear polarization.

Figure 3.12 shows a larger 2D array of ellipsoid cross-sectioned nano-structures, fabricated with linear (horizontal) polarization. The structures are confined in 2D such that the mean thicknesses are 350 nm (perpendicular to polarization) and 1200 nm (parallel to polarization).

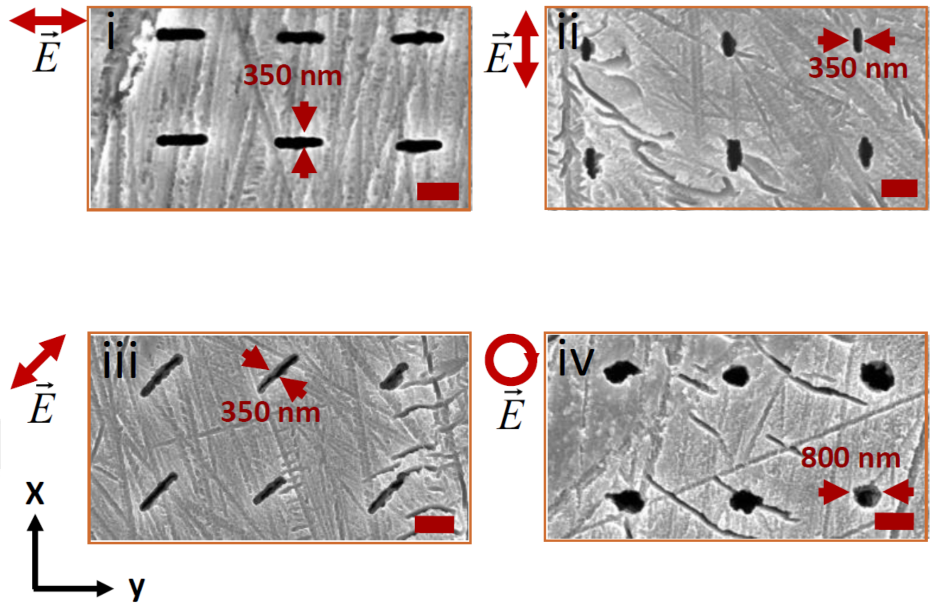

Figure 3.11: Comparison of the change in architecture of 2D-confined nano-structures under different laser polarizations. The structures are written with longitudinal scanning, using a Bessel beam of r_0 = 8 and pulse energy = 3.7 ± 0.3 μJ. All samples were etched for 30 secs to reveal the nano-structures. The scale bars are 1 μm. For linear polarization, the average thickness is found as 350 nm (perpendicular to polarization) and 1200 nm (parallel to polarization). Circularly polarized light generally creates circular structures.

In order to study whether a small change in phase can introduce a significant change in the thickness of the structures, we carried out similar experiments. We used vertical polarization, r_0= 8 and r_0= 7 and a pulse energy of 4.3 μJ. For r_0 = 7, average vertical thickness of 2D-confined structures was found to be 1500 ± 200 nm, with a horizontal thickness of 567 ± 111 nm. For r_0 = 8 the corresponding values were 1660 ± 161 nm and 518 ± 130 nm, respectively. Thus, average thicknesses were not significantly affected by the small change in phase.

Thus, while symmetric in-chip nanofabrication may require circular polarization, we can go deeper inside the nano-regime with linear polarization.

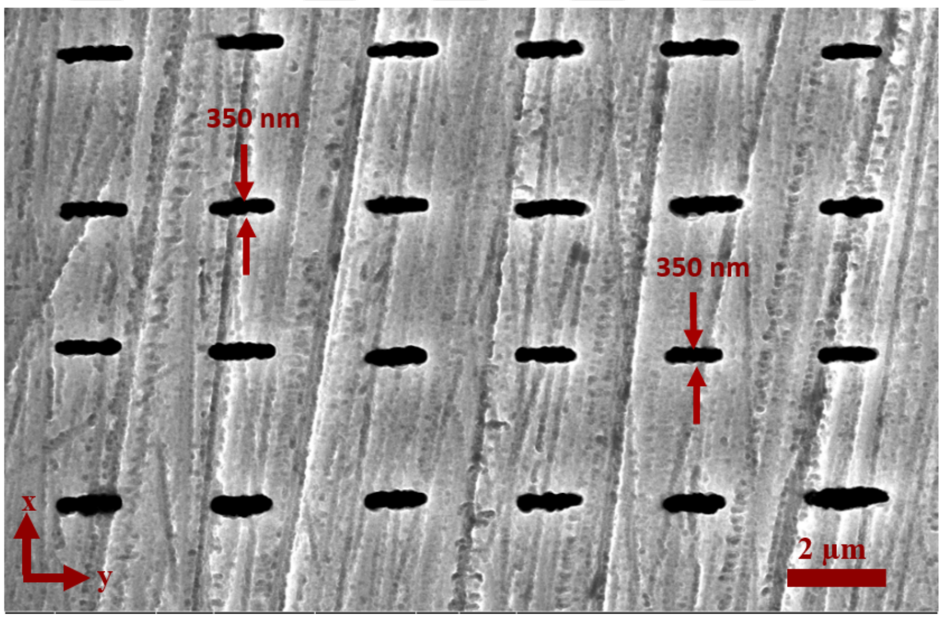

Figure 3.12: Scanning electron microscope of an in-chip 2D array of nano-structures. The in-chip array is fabricated with a Bessel beam of r_0=8, pulse energy of 3.7 $\pm$ 0.3 µJ and linear polarization (horizontal). The average thickness along the polarization axis is found as 1200 $\pm$ 100 nm, and the average thickness along the axis perpendicular to the polarization is 350 $\pm$ 30 nm.

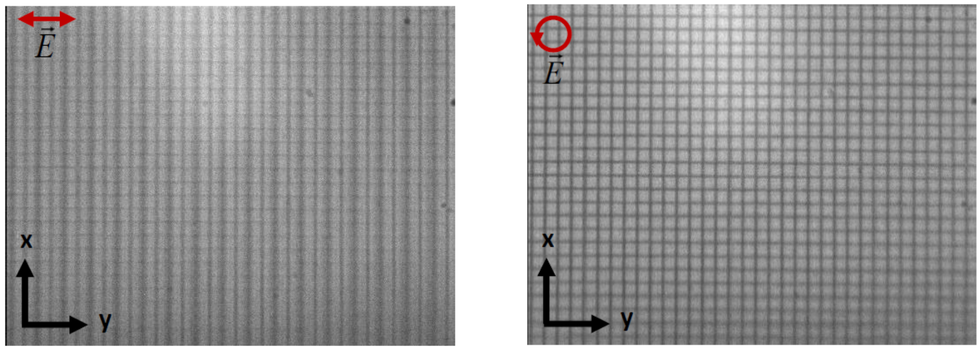

Figure 3.13: Optical transmission microscope images showing how polarization and scanning direction affect feature sizes of the in-chip modifications. On the left, the laser polarization is linear, along the y axis. On the right, the polarization is circular. In both cases, the laser propagates along z axis, the raster scans creates horizontal and vertical structures (along x and y axis).Laser parameters are: r_0 = 10, E_p = 6.7 µJ

Control over large arrays: We can use the polarization to exert control on architecture. To demonstrate this, we carried out raster scan experiments in the transverse modality and created arrays of 1D-confined in-chip planes. Figure 3.13 shows the fabrication of a rectangular-mesh array for both horizontal polarization (Figure 3.13, left) and circular polarization (Figure 3.13, right). We observed that when the scanning direction is parallel to polarization, the structure thickness is significantly lower than when the scanning direction is perpendicular to polarization. This resulted in an asymmetric mesh in the case where the polarization was linear, as seen in the left image in Figure 3.13. In contrast, when the polarization is circular, the mesh is symmetric, with no clear dependence of the structure thickness on the scanning direction (Figure 3.13,right). The result of this experiment was consistent with our earlier experiments on 2D-confined structures, and the hypothesis that we can exert an additional degree of control on feature thickness by the polarization and the scanning direction. Next, we now take a deeper look at the polarization dependent in-chip nano-fabrication.

3.4 In-chip nanofabrication in the sub-diffraction regime

So far, we identified four key parameters that can affect the feature size in 1D- and 2D-confined structures, which are polarization, pulse energy (laser power), scanning direction, and phase of the beam. Next, we optimized these parameters, to achieve a significant reduction in the feature sizes in 1D-confined structures, which ultimately allows sub-diffraction applications.

In order to carry a controlled experiment to study the impact of the phase and laser power on the in-chip modifications, we first set laser polarization to linear and parallel to scanning direction. This allows for any given power and phase (r_0), the minimum structure thickness in 1D. We then carried out a large set of experiments where the laser power is kept constant, and changed the phase of the beam by changing r_0. This set of experiments were repeated for three different pulse energies. The plot in Figure 3.14 represents our results. As expected, we observed that by decreasing both the r_0 and pulse energy, we can significantly reduce the feature size, ultimately achieving an order of magnitude reduction in the feature size from the state of the art.

We observed that both the pulse energy and phase plays a significant role in decreasing the feature size. Higher r_0 values appear to be more suited for micro-fabrication, whereas lower r_0 values ($r_0 \leq 10$) are more optimal for nanofabrication. With lower powers, the yield decreases for higher r_0 values, whereas at smaller r_0 values the sensitivity of the feature size to power is lower. In this regard, we found the optimal phase for a wider fabrication range is at r_0 = 10, with high sensitivity to power change. At lower power, deep inside the nanofabrication range, the structures are also more uniform with a standard deviation in the range of a few tens of nanometer. This is critical for high efficiency optical applications. At higher power and with higher r_0 values, the standard deviation increases significantly. This is an expected outcome since the peak intensity is higher at higher power and with larger r_0 values. This results in a larger variation of the thickness of the voxel above the modification threshold along the optical axis, creating non-uniformity along the length of the fabricated structure.

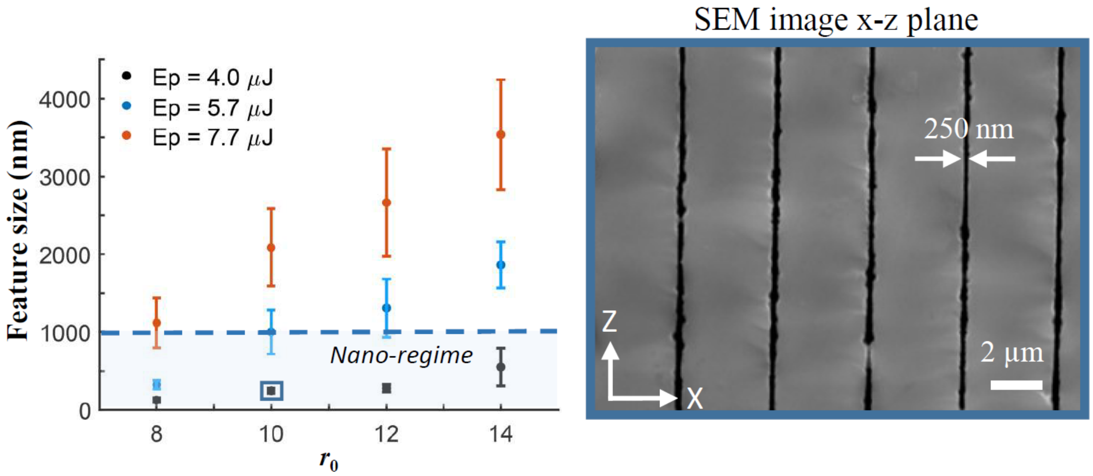

Figure 3.14: The figure shows the variation of average feature thickness with r_0 for three different pulse energies. The scanning speed =1 mm/s, repetition rate = 150 KHz, pulse duration = 8 ns, using a silicon sample of orientation <100>, and 1 mm thickness, with resistivity = 5-15 Ω.cm. On the right, SEM image of highly reproducible and uniform nanostructures created with r_0 =10 with an average thickness of 250 nm, close to the diffraction limit of light in silicon at 1.55 μm wavelength. The structures are etched for one minute to reveal the actual thickness. The polarization is p-pol (parallel to incident plane).

Now that we have been able to go deeper inside the nano-fabrication regime, it is important to consider what is the diffraction limit inside silicon. For a wavelength of 1.55 μm, and taking the refractive index of silicon to be approximately 3.47, the diffraction limit in Si becomes 224 nm. This limit is critical when operating with a Gaussian beam type, as tighter focus will be required to achieve thinner structures, which adheres by this limit. However, the unique power localization of Bessel beam have allowed us to fabricate structures that are up to 10 times thinner than the beam spot size (i.e. 250 nm thick structures obtained with a beam of spot size around 3 μm). Therefore, with further optimization, we expected to be able create structures which are thinner than the 224 nm limit in Si, opening up a new regime of sub-diffraction fabrication that can have significant implication in subwavelength nanophotonics.

Thus, we performed a set of experiments with r_0 = 10, and by changing the pulse energy, to observe how this affects the thickness and uniformity of the structures. Our experiments revealed excited results, where we were able to achieve sub-200 nm structures with remarkable uniformity (Figure 3.15).

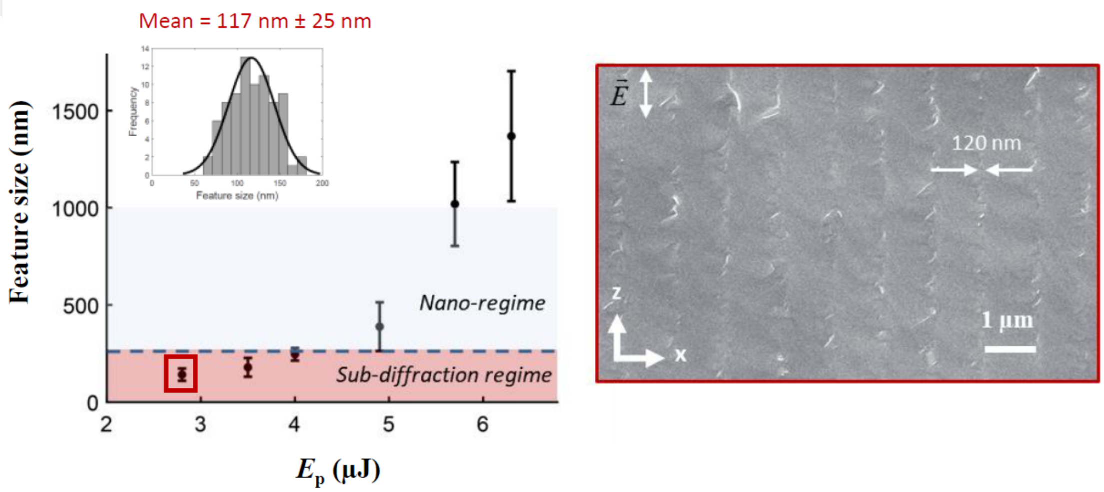

Figure 3.15: The plot of average feature size vs pulse energy for r_0 = 10, illustrating the wide range of control that can be exerted in both nano-and sub-diffraction regime. The histogram in the inset shows the size distribution for of the laser-written structures for r_0 = 10 at 2.8 μJ pulse energy, with a mean of 117 nm and standard deviation of 25 nm. To the right shows the SEM image of the first ever sub-diffraction in-chip nano-structures. The structures are separated by just 1 μm (scalebar is 1 μm). Si was imaged under SEM without etching, to preserve the exact morphology. Laser parameters were as follows: scanning speed =1 mm/s, repetition rate = 150 KHz, pulse duration = 8 ns, and with a silicon sample of orientation <100>, 1 mm thickness, resistivity = 5-15 Ω.cm. The polarization is p-pol (parallel to incident plane).

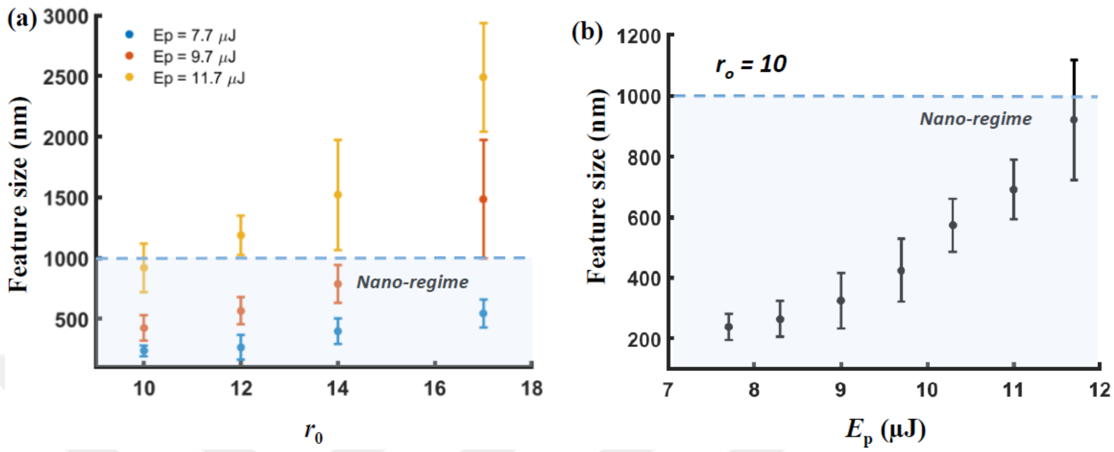

Figure 3.16: (a) The plot shows the variation of average feature thickness with r_0 for three different pulse energies. scan speed =1 mm/s, repetition rate = 150 KHz, pulse duration = 14 ns, and with a silicon sample with orientation <100>, that was 1 mm thick with resistivity = 5-15 Ω.cm. (b) The plot shows the average feature size vs. pulse energy for r_0 = 10 under the same parameters as in (a), illustrating the wide range of control that can be exerted in the nano-regime. The polarization is p-pol (parallel to incident plane).

We further carried out feature size control experiments using a higher pulse duration of 14 ns. The results (Figure 3.16) show that change in feature width with varying pulse energy and r_0 maintains the same trend, with higher pulse energy and higher r_0 values increasing the feature width. However, interestingly, the regime where nanostructuring can be achieved inside silicon is shifted to the right, requiring higher pulse energies. The minimum feature size obtained was also larger (260 nm) than that obtained with 8 ns pulse width (120 nm) for the range of our experiments, however, we expect that sub-diffraction feature sizes can be reached by scaling down the pulse energy further even at 14 ns pulse duration. This shows that the timescale plays a role in the formation of the nanostructures inside silicon, and we hypothesize that the minimum feature size can be reduced further with varying the pulse width. Future studies need to be conducted to systematically study the effects of pulse duration on the feature widths and as another direction, and the study may be expanded to laser-writing with Bessel beams in the ultrafast regime.

Chapter 4

Application of subsurface nanofabrication in Si: volume Bragg gratings

Numerous optical devices have been demonstrated inside transparent mediums by utilizing the refractive index contrast created with laser writing such as 3D optical storage devices [5, 55, 56], diffraction and Bragg gratings [7, 57, 58], and waveguides [6]. The possibility of inscribing diffraction gratings inside silicon was first suggested by Tokel et al. [5]. Chambonneau et al. demonstrated the first diffraction gratings inscribed inside silicon with nanosecond pulses [7]. The gratings had microscale pitches and a +1 order to 0 order efficiency of 10%. The possibility of fabricating the in-chip Bragg gratings in silicon was suggested in [7], but has not yet been demonstrated inside silicon. Here, we demonstrate the first in-chip Bragg-gratings with efficiencies of approaching 90%, and created with sub-micron resolution.

4.1 Theoretical background on volume Bragg gratings

Volume Bragg gratings (VBG), or volume Bragg holographic gratings are based on refractive-index modulation inside transparent media, created with low periodicity over a 3D region. VBGs can be fabricated to function either as reflection or transmission VBGs (RTVG/TVBG). In TVBG, incident light is mainly split into two transmitted orders, and when the so-called Bragg condition is met, the diffraction leads to highest efficiency. In contrast, when the Bragg condition is not met, little to no diffraction takes place. VBGs require small periodicities and significantly extended patterns, rendering their fabrication particularly challenging. Early VBGs were demonstrated in 1989 by Meltz et al. inside glass [58], and subsequent works have shown high efficiency ($> 90\%$) VBGs in fused silica [59] and photo-thermo-refractive glass [60].

We may use the following equation to identify the Bragg regime [61]:

$$L > \frac{n\Lambda^2}{2\pi\lambda} \tag{4.1}$$

Here L is the grating length, n is the refractive index of the medium, Λ is the periodicity of the grating (corresponding to the distance between two modifications) and λ is the operational wavelength. As an example, for L=260µm, and λ=1.55µm, Λ needs to be smaller than 27 µm in order for the Bragg condition to be met. In the Bragg regime, the highest diffraction efficiency is obtained when the light is incident at the Bragg angle inside the medium. The expression for the Bragg angle θ_B is [61, 62]:

$$\sin(\theta_B) = \frac{\lambda}{2\Lambda n} \tag{4.2}$$

The effectiveness of the VBG is determined based on the efficiency η, experimentally found as the ratio of the power in the diffracted beam to that of the transmitted beam. The theoretical efficiency of a VBG can be calculated according to Kogelnik's theory; if the device satisfies the exact Bragg condition ($\theta_{in} = \theta_B$), this can be expressed as [61–63]:

$$\eta = 4F^2 \sin\left(\frac{2\pi F l \Delta n}{\lambda(1-(\frac{\lambda}{2\Lambda n})^2)^{\frac{1}{2}}}\right)^2 \tag{4.3}$$

where Δn is the amplitude of refractive index modulation, and F is the filling factor, which is found by the ratio between modification width t and periodicity Λ.

4.2 Experimental results and characterization

In order to fabricate transmission volume Bragg gratings (TVBG) inside silicon, we used the transverse modality for processing, and carried out raster scans with r_0 = 7, with pulse energy = 8.7 μJ, scanning speed 1 mm/s repetition rate = 150 kHz. We used linear polarization along the sample scanning direction. The Si sample was 1 mm thick, double-side-polish, with a crystallographic orientation $< 111 >$ and resistivity 1-10 Ω.m. Bessel beam with r_0 = 7 ensured creation of nano-structures even at this higher pulse energy The ability to fabricate high-aspect-ratio in-chip nano-structures was key in fabricating the VBGs.

The separation between laser-written structures (Λ) were chosen as 1500 nm, as structure thickness was estimated to be around 750 nm. With these parameters, the grating efficiency was expected to depend on the fabrication length along laser propagation direction. In particular, highest efficiencies are expected at the Bragg angle, and this is anticipated to depend on the grating length. We confirmed this expectation simply exploiting multi-level nano-fabrication in the creation of our gratings.

A large grating area (3×3 mm^2) was required to be comparable with the characterization beam diameter. Thus, the fabrication of each layer required about 1.5 hours. The multi-layer fabrication approach is shown in Figure 4.1. The in-chip gratings were first imaged with infrared transmission microscope to verify their formation, followed by SEM images for more detailed analysis.

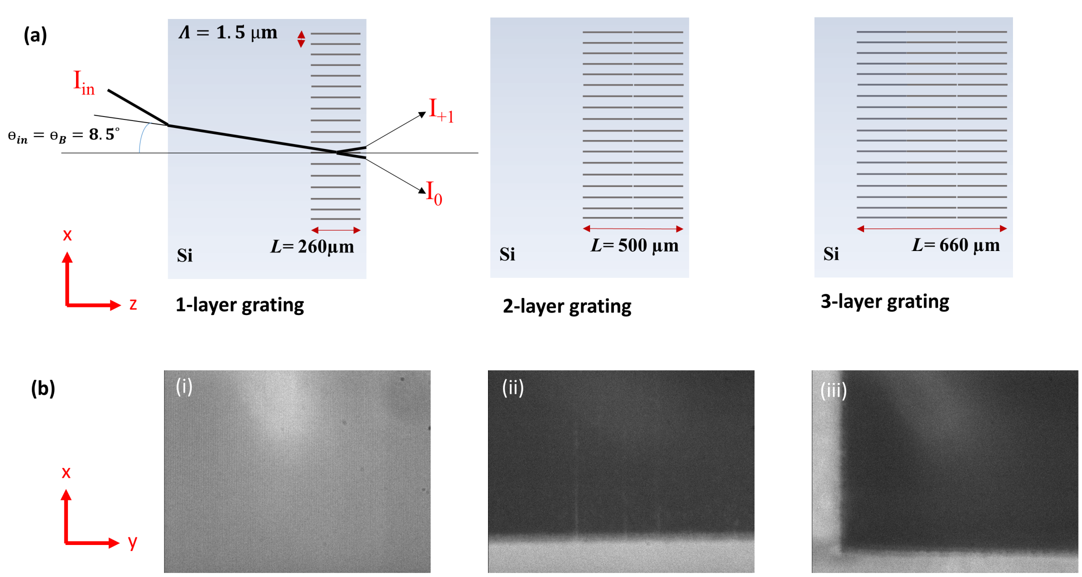

Figure 4.1: (a) The conceptual schematic showing multi-layer in-chip TVBGs with multiple layers. The layers are intentionally represented as discontinuous, but only to increase clarity. SEM images confirm continuity. (b) Infrared transmission microscope images of the samples are shown. Individual nano-planes become indistinguishable when more than one layer is fabricated.

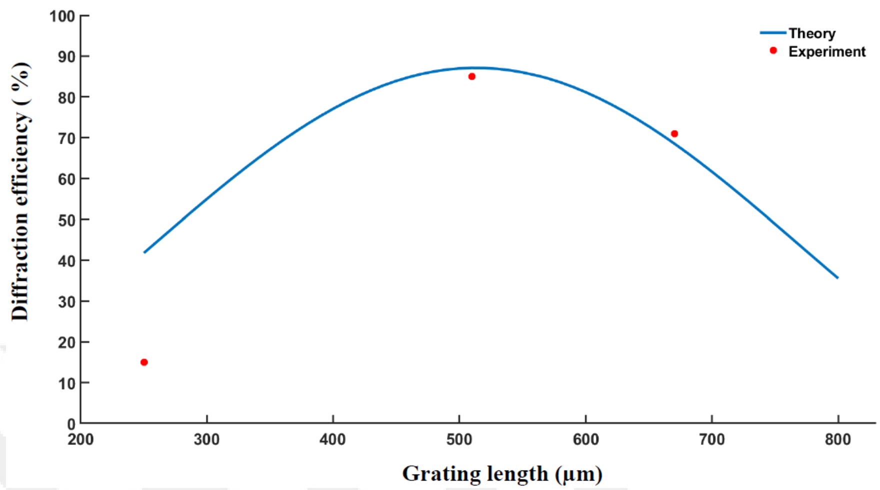

Figure 4.2: Diffraction efficiency as a function of grating length. For the theoretical value, the filling factor is assumed to be F = 0.5, average width of modifications is considered to be 750 nm wide and the estimated refractive index contrast is considered to be $\Delta n \sim 1.6 \times (10)^{-3}$. The calculated efficiencies at the Bragg angle (8.5°) for the TVBGs with single, double, and triple layers were 14%, 85% and 71% respectively.

The fabricated TVBGs were characterized at a wavelength λ = 1.55 µm, using linearly polarized light (s-polarized). In order to take into account potential losses due to scattering, we use the definition of diffraction efficiency (DE) as the ratio of the power in the $+1$ diffraction order and the power of the transmitted light as follows [61]:

$$DE = \frac{I_{+1}}{I_0 + I_{+1}} \tag{4.4}$$

Figure 4.2 shows the measured results, along with expected values from theory. We observe a reasonable match between the experimental and calculated values, in particular, for the double and triple layered gratings, assuming a refractive index contrast $\Lambda n \sim 1.6 \times (10)^{-3}$. This index contrast is consistent with the index contrast measured from Gaussian-beam written structures. In the future, an independent confirmation on the index contrast is planned, using quantitative phase microscopy. The highest grating efficiency of 85% was measured for the double-layered gratings.

The efficiency of the single-layer grating was somewhat lower than expected. To better understand the deviation from the theoretical estimate, accurate length and

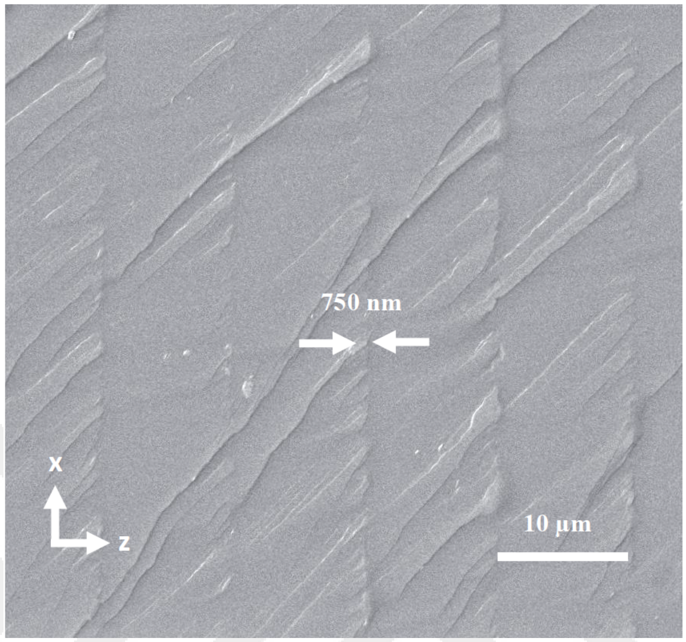

Figure 4.3: SEM image of the cross-section of the TVBG with two layers.

thicknesses were measured with SEM. Similar experiments were repeated on new samples, but with larger line separation, such as to reduce the writing time. Figure 4.3 shows the SEM image of the cross-section of a two-layer grating, with an average thickness of 743 ± 147 nm, as expected. However, for the single-layer grating, the average thickness was somewhat lower (431 ± 127 nm, revealed after 40 seconds etching), which indicated that the filling factor may not be optimal; ongoing experiments will detail this.

The demonstrated efficiency of 85% obtained with double-layer gratings is a significant first step, constituting the first proof-of-concept optical element incorporating in-chip nano-planes. These preliminary results also indicate that with further optimization, it is very likely to improve the uniformity of the laser-written structures. In particular, we found that simply by overlapping the writing areas/volumes, highly continuous in-chip nano-patterning is possible. It is also possible to control the filling factor by optimizing the phase (i.e. r_0 parameter), pulse energy and scanning conditions. Similar in-chip optics created with 1D-confined arrays may find applications as beam splitters and spectral filters, among other applications. Further, since we can reach sub-diffraction thicknesses, it should be possible to scale the grating pitch to sub-micron level, to achieve novel in-chip nano-photonics elements. In addition, 2D-confined nano-structures will also be very useful fabrication sub-components, which is an exciting future direction.

Chapter 5

Conclusion

In this thesis, a new laser-based nanofabrication approach is demonstrated with multidimensional control and sub-diffraction resolution inside silicon. The study extends the field of in-chip Si-photonics introduced in ref [5], to the nano-regime, and further explores the control of laser-written 1D-/2D-confined structures at the micro- and nano-scale.

The technique is developed using a class of 'nondiffracting' beam type, zeroth-order Bessel beam, generated using a spatial light modulator. The experiments were conducted using a master-oscillator-power-amplifier laser system operating at a wavelength of 1.55-µm, with pulses of 8 - 14 ns, and with a repetition rate of 150 KHz. The beam after the SLM is simulated and compared with experimental beam profiles. Characterization of the beam was carried out using an InGaAs camera (Artray 031TINR) at different locations along the optical axis. The experimental profile showed a close match to simulated intensity distribution, verifying the expected Bessel profile after focusing lens. For imaging and characterization of the created structures, a home-built infrared transmission microscope and a scanning electron microscope (SEM) were used. The infrared microscope was used to verify the formation of in-chip structures, and the SEM was used to accurately measure the thickness of the structures and for further data acquisition.

The laser-writing experiments were conducted in two different writing modalities. In the transverse modality the laser was scanned perpendicular to the optical axis, creating 1D-confined planes of in-chip modification. In the longitudinal modality, the laser was scanned along the optical axis, to fabricate extended cylindrical modifications, confined in 2D. The control over dimensional confinement was achieved with modulation of phase, pulse energy and laser polarization. In order to image 1D-confined structures with SEM, the sample was diced from the middle of the laser-written volume to expose buried structures, which were then imaged both before and after selective chemical etching. In order to characterize 2D-confined structures, the samples were first polished using a mechanical polishing method, which allowed us to reach the fabricated area. Then, the structures were revealed with selective chemical etching, which is followed by SEM imaging.

Our results demonstrate that we can control the feature size of in-chip structures in multiple-dimensions. As for 1-D confinement, that is created with transverse modality, we found that modulating the phase and pulse energy allows resolution control. The feature size of such structures range from a few micrometers to 600 nm, when using circular polarization. This already breaks the 1-μm limit of the state-of-the-art. Further, using linear polarization and scanning the laser in the transverse modality, we could create 1D-confined structures with down to 250 nm features (Figure 3.14). Combined with a judicious choice in scanning direction, this approach allows fabricating large-area-covering arrays in the nano-regime.

Extending the approach to 2D-confinement proved to be challenging, since we observed that laser-written structures stopped forming for $r_0 \leq 10$, even at high pulse energies, when using longitudinal-writing modality. This observation was somewhat counterintuitive, since, the same (or similar) parameters proved to be successful in creating nanostructures in the transverse modality.

Interestingly, this problem was overcome by first fabricating a 1D-confined in-chip plane (with transverse writing modality) which then enabled fabrication of 2D-confined nano-structures using longitudinal modality. Although self-seeding of laser-induced formations has been observed before, we believe this is the first observation of a proximity-type seeding effect. The effect persists over a short range of 2 μm measured from the pre-formed seed. Once a 2D-confined structure is initiated, it can be elongated virtually indefinitely, even to distances away from the seed, meaning that the 2D-confined structures can be exploited at depths where there is no preformed seed element. Using this technique, observed symmetric structures could be scaled down to 600 nm with circular polarization, similar to our results of 1D-confinement with circular polarization.

Further, linear polarization allowed creation of slightly oblique 2-D confined structures and even smaller feature sizes were possible. We investigated the effect of polarization on the formation and architecture of 2D-confined structures with four sets of experiments. At a particular parameter set, we performed experiments with circular, horizontal and vertical polarization, as well as 45° polarization. We found that structures created with circular polarization were symmetric, with a diameter of 800 nm. In contrast, for all linear polarization cases, the structures were asymmetric, but confined in a space perpendicular to the direction of the polarization. This corresponds to an elliptical or rod-like shape. The minimum thickness was 350 nm for all cases, observed along the axis perpendicular to polarization. This indicated that it is possible to reduce the thickness, if the polarization is switched from circular to linear. This observation is consistent with the fact that circular polarization is a superposition of the horizontal and vertical polarization, and its symmetry is correspondingly making in-chip structures more symmetric, but slightly larger.

The results of the preceding observations motivated us to push the feature size even lower, from the 600-nm-sized, 1D-confined structures, to the sub-diffraction regime of < 220 nm. A systematic set of experiments were performed with linear polarization, transverse-writing modality, and with different r_0 values (phase modulation) and pulse energies. We were able to reproducibly fabricate 1D-confined in-chip nanostructures of tunable feature thickness, ranging from a few micrometers down to 120 nm (r_0 = 10, pulse energy = 2.8 μJ). This was achieved by reducing the effective core diameter of the Bessel beam, keeping the laser power very close to the modification threshold.

In summary, for 1-D confinement, we have achieved beyond-diffraction-limit feature sizes (120 nm), and in the 2D-confinement, we have achieved down to 350 nm, both constituting the state-of-the-art for in-chip fabrication. We achieve in-chip nanofabrication on the technologically important material, Si, with subwavelength refractive index modulation. We believe this new capability has the potential to open exciting opportunities for in-chip nano-photonics devices. As proof-of-concept demonstration we applied this capability to demonstrate an in-chip volumetric Bragg grating, achieving a maximum efficiency of 85%. The implication for novel nano-photonics devices is exciting. In-chip nanofabrication also has potentially significant applications in micro/nano-fluidics, micro/nano-optoelectronic and optomechanical devices.

Bibliography

[1] A. Rickman, "The commercialization of silicon photonics," *Nature Photonics*, vol. 8, no. 8, pp. 579–582, 2014.

[2] M. Lipson, "Guiding, modulating, and emitting light on silicon-challenges and opportunities," *Journal of Lightwave Technology*, vol. 23, no. 12, p. 4222, 2005.

[3] M. A. Foster, R. Salem, D. F. Geraghty, A. C. Turner-Foster, M. Lipson, and A. L. Gaeta, "Silicon-chip-based ultrafast optical oscilloscope," *Nature*, vol. 456, no. 7218, pp. 81–84, 2008.

[4] M. Chanal, V. Y. Fedorov, M. Chambonneau, R. Clady, S. Tzortzakis, and D. Grojo, "Crossing the threshold of ultrafast laser writing in bulk silicon," *Nature communications*, vol. 8, no. 1, pp. 1–6, 2017.

[5] O. Tokel, A. Turnalı, G. Makey, P. Elahi, T. Çolakoğlu, E. Ergeçen, Ö. Yavuz, R. Hübner, M. Z. Borra, I. Pavlov, *et al.*, "In-chip microstructures and photonic devices fabricated by nonlinear laser lithography deep inside silicon," *Nature photonics*, vol. 11, no. 10, pp. 639–645, 2017.

[6] A. Turnali, M. Han, and O. Tokel, "Laser-written depressed-cladding waveguides deep inside bulk silicon," *JOSA B*, vol. 36, no. 4, pp. 966–970, 2019.

[7] M. Chambonneau, D. Richter, S. Nolte, and D. Grojo, "Inscribing diffraction gratings in bulk silicon with nanosecond laser pulses," *Optics Letters*, vol. 43, no. 24, pp. 6069–6072, 2018.

[8] G. Makey, Ö. Yavuz, D. K. Kesim, A. Turnalı, P. Elahi, S. Ilday, O. Tokel, and F. Ö. Ilday, "Breaking crosstalk limits to dynamic holography using orthogonality of

high-dimensional random vectors," *Nature photonics*, vol. 13, no. 4, pp. 251–256, 2019.

[9] K. M. Davis, K. Miura, N. Sugimoto, and K. Hirao, "Writing waveguides in glass with a femtosecond laser," *Optics letters*, vol. 21, no. 21, pp. 1729–1731, 1996.

[10] Y. Bellouard, A. Said, M. Dugan, and P. Bado, "Fabrication of high-aspect ratio, micro-fluidic channels and tunnels using femtosecond laser pulses and chemical etching," *Optics express*, vol. 12, no. 10, pp. 2120–2129, 2004.

[11] Y. Bellouard, A. Champion, B. Lenssen, M. Matteucci, A. Schaap, M. Beresna, C. Corbari, M. Gecevičius, P. Kazansky, O. Chappuis, *et al.*, "The femtoprint project," *Journal of Laser Micro/Nanoengineering*, vol. 7, no. 1, pp. 1–10, 2012.

[12] R. R. Gattass and E. Mazur, "Femtosecond laser micromachining in transparent materials," *Nature photonics*, vol. 2, no. 4, pp. 219–225, 2008.

[13] A. Vorobyev and C. Guo, "Laser turns silicon superwicking," *Optics Express*, vol. 18, no. 7, pp. 6455–6460, 2010.

[14] S. Großer, D. Lausch, M. Werner, S. Swatek, M. Mergner, V. Naumann, and C. Hagendorf, "Shunt analysis in solar cells-electro-optical classification and high resolution defect diagnostics," *Energy Procedia*, vol. 27, pp. 7–12, 2012.

[15] R. Khrapko, C. Lai, J. Casey, W. A. Wood, and N. F. Borrelli, "Accumulated self-focusing of ultraviolet light in silica glass," *Applied Physics Letters*, vol. 105, no. 24, p. 244110, 2014.

[16] A. Couairon and A. Mysyrowicz, "Femtosecond filamentation in transparent media," *Physics reports*, vol. 441, no. 2-4, pp. 47–189, 2007.

[17] A. H. Nejadmalayeri, P. R. Herman, J. Burghoff, M. Will, S. Nolte, and A. Tünnermann, "Inscription of optical waveguides in crystalline silicon by mid-infrared femtosecond laser pulses," *Optics Letters*, vol. 30, no. 9, pp. 964–966, 2005.

[18] Y. Ito, H. Sakashita, R. Suzuki, M. Uewada, K. P. Luong, and R. Tanabe, "Modification and machining on back surface of a silicon substrate by femtosecond laser pulses at 1552 nm," *Journal of Laser Micro Nanoengineering*, vol. 9, no. 2, p. 98, 2014.

[19] V. V. Kononenko, V. V. Konov, and E. M. Dianov, "Delocalization of femtosecond radiation in silicon," *Optics letters*, vol. 37, no. 16, pp. 3369–3371, 2012.

[20] O. Tokel, I. Pavlov, I. Akca, S. Tozburun, A. Turnali, and F. O. Ilday, "Laser-writing in silicon for 3d information processing," tech. rep., 2014.

[21] A. Turnali, O. Tokel, I. Pavlov, and F. Ö. Ilday, "Direct laser writing of volume fresnel zone plates in silicon," in *The European Conference on Lasers and Electro-Optics*, p. CM_4_5, Optical Society of America, 2015.

[22] O. Tokel, A. Turnalı, I. Pavlov, and F. Ö. Ilday, "Laser writing deep inside silicon for 3d information processing," in *The European Conference on Lasers and Electro-Optics*, p. CK_P_34, Optical Society of America, 2015.

[23] M. Chambonneau, Q. Li, M. Chanal, N. Sanner, and D. Grojo, "Writing waveguides inside monolithic crystalline silicon with nanosecond laser pulses," *Optics letters*, vol. 41, no. 21, pp. 4875–4878, 2016.

[24] I. Pavlov, O. Tokel, S. Pavlova, V. Kadan, G. Makey, A. Turnali, Ö. Yavuz, and F. Ilday, "Femtosecond laser written waveguides deep inside silicon," *Optics Letters*, vol. 42, no. 15, pp. 3028–3031, 2017.

[25] X. Yu, X. Wang, M. Chanal, C. A. Trallero-Herrero, D. Grojo, and S. Lei, "Internal modification of intrinsic and doped silicon using infrared nanosecond laser," *Applied Physics A*, vol. 122, no. 12, p. 1001, 2016.

[26] E. G. Gamaly, S. Juodkazis, K. Nishimura, H. Misawa, B. Luther-Davies, L. Hallo, P. Nicolai, and V. T. Tikhonchuk, "Laser-matter interaction in the bulk of a transparent solid: Confined microexplosion and void formation," *Physical Review B*, vol. 73, no. 21, p. 214101, 2006.

[27] Q. Li, M. Chambonneau, M. Chanal, and D. Grojo, "Quantitative-phase microscopy of nanosecond laser-induced micro-modifications inside silicon," *Applied optics*, vol. 55, no. 33, pp. 9577–9583, 2016.

[28] O. V. Angelsky, A. Y. Bekshaev, S. G. Hanson, C. Y. Zenkova, I. I. Mokhun, and Z. Jun, "Structured light: ideas and concepts," *Front. Phys. 8: 114. doi: 10.3389/fphy*, 2020.

[29] C. Tamm and C. Weiss, "Bistability and optical switching of spatial patterns in a laser," *JOSA B*, vol. 7, no. 6, pp. 1034–1038, 1990.

[30] L. Allen, M. W. Beijersbergen, R. Spreeuw, and J. Woerdman, "Orbital angular momentum of light and the transformation of laguerre-gaussian laser modes," *Physical review A*, vol. 45, no. 11, p. 8185, 1992.

[31] M. Harris, C. Hill, and J. Vaughan, "Optical helices and spiral interference fringes," *Optics communications*, vol. 106, no. 4-6, pp. 161–166, 1994.

[32] V. G. Shvedov, A. S. Desyatnikov, A. V. Rode, W. Krolikowski, and Y. S. Kivshar, "Optical guiding of absorbing nanoclusters in air," *Optics Express*, vol. 17, no. 7, pp. 5743–5757, 2009.

[33] V. G. Shvedov, A. V. Rode, Y. V. Izdebskaya, A. S. Desyatnikov, W. Krolikowski, and Y. S. Kivshar, "Giant optical manipulation," *Physical review letters*, vol. 105, no. 11, p. 118103, 2010.

[34] M. Padgett and R. Bowman, "Tweezers with a twist," *Nature photonics*, vol. 5, no. 6, pp. 343–348, 2011.

[35] V. Garcés-Chávez, D. McGloin, M. Padgett, W. Dultz, H. Schmitzer, and K. Dholakia, "Observation of the transfer of the local angular momentum density of a multiringed light beam to an optically trapped particle," *Physical review letters*, vol. 91, no. 9, p. 093602, 2003.

[36] B. K. Singh, H. Nagar, Y. Roichman, and A. Arie, "Particle manipulation beyond the diffraction limit using structured super-oscillating light beams," *Light: Science & Applications*, vol. 6, no. 9, pp. e17050–e17050, 2017.

[37] F. J. Rodríguez-Fortuño, G. Marino, P. Ginzburg, D. O'Connor, A. Martínez, G. A. Wurtz, and A. V. Zayats, "Near-field interference for the unidirectional excitation of electromagnetic guided modes," *Science*, vol. 340, no. 6130, pp. 328–330, 2013.

[38] X.-L. Wang, X.-D. Cai, Z.-E. Su, M.-C. Chen, D. Wu, L. Li, N.-L. Liu, C.-Y. Lu, and J.-W. Pan, "Quantum teleportation of multiple degrees of freedom of a single photon," *Nature*, vol. 518, no. 7540, pp. 516–519, 2015.

[39] C. Hnatovsky, V. G. Shvedov, and W. Krolikowski, "The role of light-induced nanostructures in femtosecond laser micromachining with vector and scalar pulses," *Optics express*, vol. 21, no. 10, pp. 12651–12656, 2013.

[40] J. Durnin, J. Miceli Jr, and J. Eberly, "Diffraction-free beams," *Physical review letters*, vol. 58, no. 15, p. 1499, 1987.

[41] R. Bowman, N. Muller, X. Zambrana-Puyalto, O. Jedrkiewicz, P. Di Trapani, and M. Padgett, "Efficient generation of bessel beam arrays by means of an slm," *The European Physical Journal Special Topics*, vol. 199, no. 1, pp. 159–166, 2011.

[42] M. Bhuyan, F. Courvoisier, P. Lacourt, M. Jacquot, R. Salut, L. Furfaro, and J. Dudley, "High aspect ratio nanochannel machining using single shot femtosecond bessel beams," *Applied Physics Letters*, vol. 97, no. 8, p. 081102, 2010.

[43] R. Meyer, M. Jacquot, R. Giust, J. Safioui, L. Rapp, L. Furfaro, P.-A. Lacourt, J. M. Dudley, and F. Courvoisier, "Single-shot ultrafast laser processing of high-aspect-ratio nanochannels using elliptical bessel beams," *Optics letters*, vol. 42, no. 21, pp. 4307–4310, 2017.

[44] D. Grojo, A. Mouskeftaras, P. Delaporte, and S. Lei, "Limitations to laser machining of silicon using femtosecond micro-bessel beams in the infrared," *Journal of Applied Physics*, vol. 117, no. 15, p. 153105, 2015.

[45] H. Cheng, C. Xia, S. M. Kuebler, and X. Yu, "Aberration correction for slm-generated bessel beams propagating through tilted interfaces," *Optics Communications*, vol. 475, p. 126213, 2020.

[46] Z. Zhai, Z. Cheng, Q. Lv, and X. Wang, "Tunable axicons generated by spatial light modulator with high-level phase computer-generated holograms," *Applied Sciences*, vol. 10, no. 15, p. 5127, 2020.

[47] J. Dudutis, P. GeČys, and G. RaČiukaitis, "Non-ideal axicon-generated bessel beam application for intra-volume glass modification," *Optics express*, vol. 24, no. 25, pp. 28433–28443, 2016.

[48] Z. Huang, N. Geyer, P. Werner, J. De Boor, and U. Gösele, "Metal-assisted chemical etching of silicon: a review: in memory of prof. ulrich gösele," *Advanced materials*, vol. 23, no. 2, pp. 285–308, 2011.

[49] B. Schwartz and H. Robbins, "Chemical etching of silicon: Iv. etching technology," *Journal of the electrochemical society*, vol. 123, no. 12, p. 1903, 1976.

[50] D. Turner, "On the mechanism of chemically etching germanium and silicon," *Journal of the electrochemical Society*, vol. 107, no. 10, p. 810, 1960.

[51] H. Idrisi, *Development of decoration and preferential-etching methods for delineation of crystal defects in semiconductor materials.* PhD thesis, Univ.-Bibliothek, 2013.

[52] A. Abbadie, J.-M. Hartmann, and F. Brunier, "A review of different and promising defect etching techniques: From si to ge," *ECS Transactions*, vol. 10, no. 1, p. 3, 2007.

[53] A. Das, A. Wang, O. Uteza, and D. Grojo, "Pulse-duration dependence of laser-induced modifications inside silicon," *Optics Express*, vol. 28, no. 18, pp. 26623–26635, 2020.

[54] A. Turnalı, *Three dimensional processing of silicon with pulsed lasers for optical applications.* PhD thesis, Bilkent University, 2015.

[55] E. Glezer, M. Milosavljevic, L. Huang, R. Finlay, T.-H. Her, J. P. Callan, and E. Mazur, "Three-dimensional optical storage inside transparent materials," *Optics letters*, vol. 21, no. 24, pp. 2023–2025, 1996.

[56] D. A. Parthenopoulos and P. M. Rentzepis, "Three-dimensional optical storage memory," *Science*, vol. 245, no. 4920, pp. 843–845, 1989.

[57] Q.-Z. Zhao, J.-R. Qiu, X.-W. Jiang, C.-J. Zhao, and C.-S. Zhu, "Fabrication of internal diffraction gratings in calcium fluoride crystals by a focused femtosecond laser," *Optics express*, vol. 12, no. 5, pp. 742–746, 2004.

[58] G. Meltz, W. Morey, and W. Glenn, "Formation of bragg gratings in optical fibers by a transverse holographic method," *Optics letters*, vol. 14, no. 15, pp. 823–825, 1989.

[59] M. Mikutis, T. Kudrius, G. Šlekys, D. Paipulas, and S. Juodkazis, "High 90% efficiency bragg gratings formed in fused silica by femtosecond gauss-bessel laser beams," *Optical Materials Express*, vol. 3, no. 11, pp. 1862–1871, 2013.

[60] O. M. Efimov, L. B. Glebov, L. N. Glebova, K. C. Richardson, and V. I. Smirnov, "High-efficiency bragg gratings in photothermorefractive glass," *Applied optics*, vol. 38, no. 4, pp. 619–627, 1999.

[61] P.-A. Blanche, P. Gailly, S. L. Habraken, P. C. Lemaire, and C. A. Jamar, "Volume phase holographic gratings: large size and high diffraction efficiency," *optical Engineering*, vol. 43, no. 11, pp. 2603–2613, 2004.

[62] I. K. Baldry, J. Bland-Hawthorn, and J. Robertson, "Volume phase holographic gratings: polarization properties and diffraction efficiency," *Publications of the Astronomical Society of the Pacific*, vol. 116, no. 819, p. 403, 2004.

[63] A. Martínez, M. del Mar Sánchez-López, and I. Moreno, "Phasor analysis of binary diffraction gratings with different fill factors," *European journal of physics*, vol. 28, no. 5, p. 805, 2007.